nature microbiology

Article

https://doi.org/10.1038/s41564-025-02161-x

Structures of the sheathed flagellum reveal mechanisms of assembly and rotation in *Vibrio cholerae*

Received: 24 April 2025

Accepted: 22 September 2025

Published online: 31 October 2025

Check for updates

Wangbiao Guo[1,2,9] ✉, Sarah Zhang[3,9], Jin Hwan Park[4], Venus Stanton[5], Merrill Asp[6,7], Helen Herrera[5], Jung-Shen Benny Tai[6,7], Jian Yue[1,2], Jiaqi Wang[1,2], Jiaqi Guo[1,2], Rajeev Kumar[1,2], Jack M. Botting[1,2], Shenping Wu[8], Jing Yan[6,7], Karl E. Klose[5], Fitnat H. Yildiz[4] & Jun Liu[1,2] ✉

Motility promotes the complex life cycle and infectious capabilities of *Vibrio cholerae* and is driven by rotation of a single polar flagellum. The flagellar filament comprises four flagellin proteins (FlaA–D) and is covered by a membranous sheath continuous with the outer membrane. Here we combine in situ cryo-electron microscopy single-particle analysis, fluorescence microscopy and molecular genetics to determine 2.92–3.43 Å structures of the sheathed flagellar filament from intact bacteria. Our data reveal the spatial arrangement of FlaA–D, showing that FlaA localizes at the cell pole and functions as a template for filament assembly involving multiple flagellins. Unlike unsheathed flagellar filaments, the sheathed filament from *V. cholerae* possesses a highly conserved core but a smooth, hydrophilic surface adjacent to the membranous sheath. A tiny conformational change at the single flagellin level results in a supercoiled filament and curved membranous sheath, supporting a model wherein the filament rotates separately from the sheath, enabling the distinct motility of *V. cholerae*.

Vibrio cholerae is a highly motile Gram-negative bacterium characterized by a comma shape and a unipolar sheathed flagellum[1]. It is the causative agent of the severe diarrhoeal disease cholera[2,3], responsible for seven global pandemics over the past two centuries as well as approximately 2.9 million cholera cases and 95,000 deaths worldwide each year[4]. The World Health Organization classified the global resurgence of cholera as a grade 3 health emergency, the highest level, due to the increasing number and geographic expansion of outbreaks, with an estimated 1.3 billion people at risk worldwide[4]. To enable the explosive spread of cholera during outbreaks and persistence during non-epidemic periods[5], *V. cholerae* has evolved remarkable mechanisms to persist and transition between the aquatic environment and human hosts during its complex life cycle. Particularly critical to *V. cholerae* pathogenesis is its motility, which enables the bacteria to effectively penetrate thick intestinal mucus and cause infection of the host[6]. As motility plays crucial roles in infection by *V. cholerae*, effective cholera vaccines produce antibodies to inhibit motility and infection[7,8].

Swimming motility in *V. cholerae* is achieved through rotation of a unipolar flagellum covered by a membranous sheath extending from the outer membrane. Powered by a sodium-motive force across the cytoplasmic membrane, the sheathed flagellum can rotate up to 1,700 Hz in liquid environments[9]. The resulting propulsive force

[1]Department of Microbial Pathogenesis, Yale School of Medicine, New Haven, CT, USA. [2]Microbial Sciences Institute, Yale University, West Haven, CT, USA. [3]Beverly Hills High School, Beverly Hills, CA, USA. [4]Department of Microbiology and Environmental Toxicology, University of California, Santa Cruz, CA, USA. [5]South Texas Center for Emerging Infectious Diseases, Department of Molecular Microbiology and Immunology, University of Texas San Antonio, San Antonio, TX, USA. [6]Department of Molecular, Cellular and Developmental Biology, Yale University, New Haven, CT, USA. [7]Quantitative Biology Institute, Yale University, New Haven, CT, USA. [8]Department of Pharmacology, Yale University, New Haven, CT, USA. [9]These authors contributed equally: Wangbiao Guo, Sarah Zhang. ✉e-mail: wangbiao.guo@yale.edu; jliu@yale.edu

https://doi.org/10.1038/s41564-025-02161-x

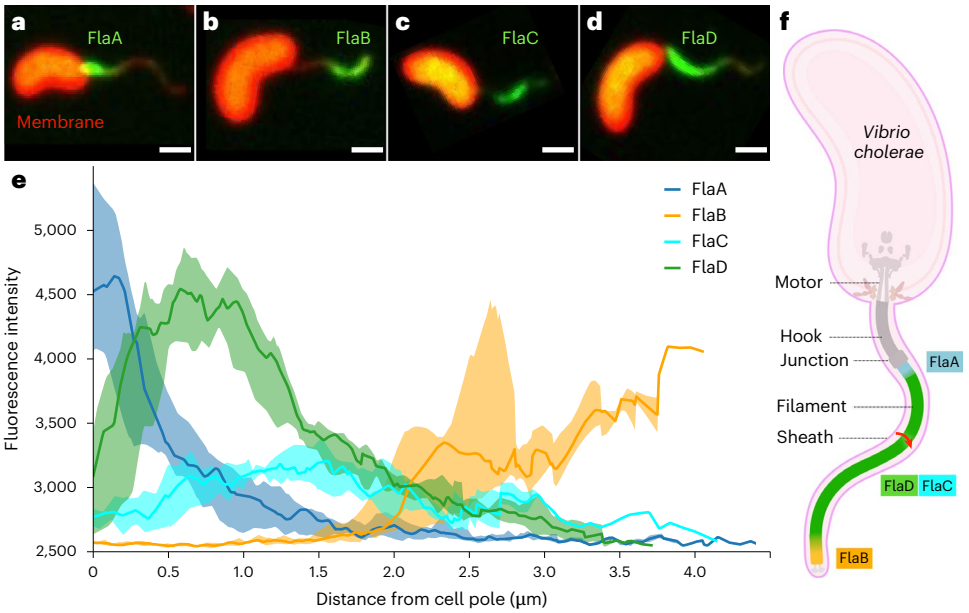

Fig. 1 | Four flagellins are localized to different zones of the sheathed flagellar filaments in *V. cholerae*. **a**–**d**, Overlay images of cell membrane stained with FM 1-63 (pseudocoloured red) and signals from each cysteine-labelled flagellin stained with Alexa Fluor 488 through maleimide coupling reaction (green); the representative images were independently repeated at least three times with similar results: FlaA localizes close to the cell pole (**a**); FlaB localizes at the end of the filament (**b**); FlaC is located primarily in the middle of the filament (**c**); FlaD is present in the middle of the flagellum, weighted more towards the cell pole (**d**). Scale bar, 1 μm. **e**, Statistics of the flagellin distribution. Solid lines are the median values of raw fluorescence data measured from eight to ten cells, and coloured bands mark the 25th and 75th percentiles, that is, half of the data around the median. **f**, A cartoon model of *V. cholerae* shows the flagellar filament and its flagellin distribution inside the membranous sheath contiguous with the outer membrane.

enables *Vibrio* to swim at speeds up to 90 μm s^{-1}, considerably faster than most bacteria[10]. The polar sheathed flagellum is composed of a motor, hook and filament covered by a membranous sheath. As the largest component of the sheathed flagellum, the filament is composed of multiple different flagellin proteins with a significant 61–82% shared identity[11]. Among the four flagellins (FlaA to FlaD) detected from purified flagella, FlaC and FlaD are the most abundant subunits of the filament[12]. However, FlaA is the only flagellin essential for flagellar synthesis and motility in *V. cholerae*[11]. The fifth flagellin, FlaE, is not directly involved in filament formation but is instead secreted into the biofilm matrix[13]. Intriguingly, these flagellins are differentially regulated by *V. cholerae*, probably enabling assembly of flagellar filaments suitable for generating motility in different environments as well as providing antigenic variation to the filaments[11].

Although unsheathed flagella have been extensively characterized by cryo-electron microscopy (cryo-EM) and helical reconstruction[14–17], sheathed flagella remain poorly understood at the molecular level[18]. Two longstanding questions remain: how do multiple flagellin proteins coordinate filament assembly within the membranous sheath[11], and how does the sheathed flagellum rotate[19]? To solve these puzzles, here we combine in situ cryo-EM[20,21] with fluorescence microscopy and molecular genetics to investigate sheathed flagella in *V. cholerae*. We determine spatial arrangement and near-atomic structures of four distinct flagellins along the filament. Our study provides insights into the assembly and function of sheathed flagella and lays the foundation for developing strategies to inhibit *V. cholerae* infection.

Results

Spatial arrangement of flagellins in the sheathed flagellum

The four flagellin proteins (FlaA–D) share highly similar sequences and only subtle structural differences (Extended Data Fig. 1). To understand how these four flagellin proteins are distributed along the *V. cholerae* sheathed flagellum, we generated four mutant strains (Supplementary Table 1), each expressing one flagellin variant containing two cysteine substitutions at equivalent positions[22]. The other three flagellins, as well as the rest of the genome, remained wild type, except for the constitutive expression of mScarlet-I at a neutral locus for imaging purposes. The strains were stained with a fluorescent, cysteine-reactive maleimide, and fluorescence intensity was subsequently quantified along the flagellum. Each flagellin consistently localizes to specific regions of the sheathed filament (Fig. 1a–e). The FlaA signal is highest at the cell pole, decaying sharply along the length of the filament, although small amounts of FlaA may be interspersed throughout the filament (Fig. 1a,e). This result is consistent with the critical role of FlaA in initiating flagellar synthesis[11]. FlaB appears to localize at the filament tip, while FlaC is distributed along the filament (Fig. 1b,c). FlaD is the predominant flagellin and has the strongest signal along the filament (Fig. 1d), with its peak distribution located between that of FlaA and FlaB. Collectively, our fluorescence microscopy data reveal the distinct spatial locations of the four flagellins along the flagellar filament as well as enable us to propose a flagellar filament model in which FlaA is located at the proximal end, FlaB forms the distal end, and FlaC and FlaD form the middle of the filament (Fig. 1f).

Cryo-EM structure of the sheathed flagellum in *V. cholerae*

To better understand how these four flagellin proteins form the filament in *V. cholerae*, we used cryo-EM to determine the in situ structure of the sheathed flagellum in intact cells. As wild-type *V. cholerae* possesses only a single flagellum at one of two poles (Fig. 2a), we constructed a *V. cholerae* Δ*flhG* mutant that produces hyperflagellated cells[23] (Fig. 2b,c and Supplementary Table 2). A total of 2,145 cryo-EM images along flagellar filaments (Fig. 2c and Supplementary Table 3) were acquired and then analysed in cryoSPARC[24] (Extended Data Fig. 2). Through extensive classification, alignment and helical refinement, we determined a helical reconstruction of the sheathed flagellar filament with helical rise 4.74 Å and twist 65.41° (Extended Data Fig. 2 and Supplementary Table 3).

As the flagellar filaments from intact bacteria exist in different polymorphic forms with various curvatures (Fig. 2a–c), we deployed an asymmetrical reconstruction approach, as described previously[14],

https://doi.org/10.1038/s41564-025-02161-x

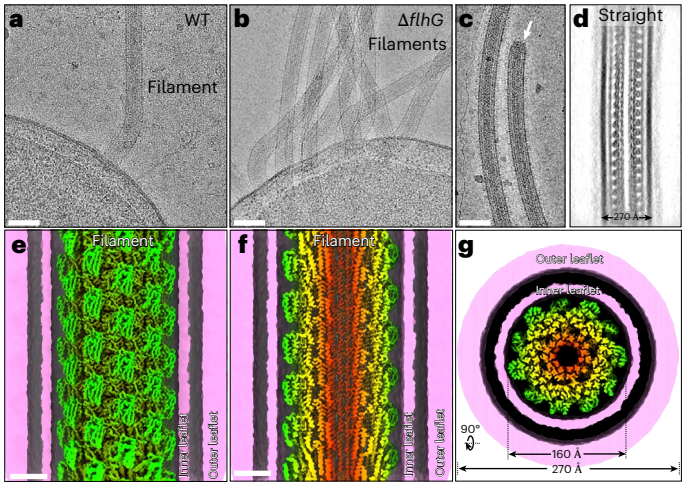

Fig. 2 | In situ cryo-EM reveals the sheathed flagellar filament structure at near-atomic resolution in *V. cholerae*. **a**,**b**, Cryo-EM images from cell tips of wild-type (WT) (**a**) and Δ*flhG* mutant (**b**) cells. The flagellar filaments are surrounded by the membranous sheath extended from the outer membrane. **c**, A cryo-EM image showing the distal end of the filament (white arrow). LPS is readily visible on the surface of the membranous sheath. The representative images were acquired independently at least three times, with thousands of comparable images supporting the findings. Scale bar, 500 Å. **d**, A class average of the straight sheathed filament with a diameter of 270 Å. The inner leaflet of the membranous sheath is significantly thinner than the outer leaflet. **e**, A side view of the cryo-EM structure of the straight sheathed filament at 2.92 Å resolution. The filament is differently coloured from the lumen to the surface. A cross-section of the membranous sheath shows the inner leaflet and outer leaflet of the membrane (pink). **f**, A cross-section of the filament structure shows the filament core. Scale bar, 50 Å. **g**, A perpendicular cross-section of the filament structure shows the hollow, tubular filament core surrounded by the membranous sheath. The diameter of the filament core is 160 Å. The diameter of the membranous sheath is 270 Å.

to determine a 2.92 Å in situ structure of the straight flagellar filament without applying helical symmetry (Fig. 2d–g and Extended Data Fig. 2). The filament with a diameter of 160 Å consists of 11 right-handed protofilaments. The lumen of the filament is 40 Å in width, and the surface is surrounded by the membranous sheath with a diameter of 270 Å (Fig. 2g). Notably, the two leaflets of the membrane are clearly visible: the inner leaflet appears relatively thin, while the outer leaflet is thicker. This observation is consistent with previous reports that the membranous sheath is an extension of the outer membrane, with lipopolysaccharide (LPS) in the outer leaflet and phospholipids in the inner leaflet[25,26].

In situ structure of the FlaD filament

Our 2.92 Å in situ structure of the straight flagellar filament enabled us to unambiguously build a model of flagellin FlaD (Fig. 3a,b). Although our fluorescence microscopy data indicate that four homologous flagellin proteins are involved in assembling the flagellar filament (Fig. 1), FlaD appears to be the major filament component in *V. cholerae* (Fig. 1e) because other models of flagellins (FlaA, FlaB and FlaC) do not fit well into the in situ structure, at least for some key residues (Extended Data Fig. 3). The FlaD monomer model can be subdivided into three structural domains: two conserved inner core domains, D0 and D1, and one outer domain, D2 (Fig. 3a).

To understand the mechanism of filament assembly, we constructed a straight FlaD filament model (Fig. 3b) that shares many similar features with other bacterial species[14,27] (Extended Data Fig. 4 and Supplementary Table 4). Our structures suggest that multiple interactions at the conserved D0 and D1 domains along the 11-start protofilament are similar to those in other bacterial species (Extended Data Fig. 5). Specifically, D94 in the N_0 subunit interacts with R59 in the N_{11} subunit, and D323 in N_0 makes contact with R16 in N_{11}. N330 and E327 in N_0 probably interact with M12 in the N_{11} subunit (Extended Data Fig. 5). Several conserved interactions at the 5-start interface are also similar to those found in *Pseudomonas aeruginosa*, *Salmonella* Typhimurium and *Campylobacter jejuni* (Extended Data Fig. 6). Therefore, the polar sheathed flagellum in *V. cholerae* shares features with unsheathed flagella in other bacterial species: a highly conserved filament core (D0 and D1 domains) and similar protein–protein interactions for filament assembly.

Sheet-and-helix motif forms a hydrophilic filament surface

D2 domains of flagellins from different species are highly variable (Extended Data Fig. 4). The D2 domains in *V. cholerae* flagellins are located at the flagellar filament surface (Fig. 3c,e and Extended Data Fig. 4). Specifically, residues 194–212 and 255–258 in the D2 domain form a three-stranded β-sheet (β8, β4 and β5) (Fig. 3c–f), and residues 259–267 form a helix (H5) (Fig. 3d and Supplementary Video 1). The sheet-and-helix motif forms a smooth and hydrophilic filament surface adjacent to the inner leaflet of the membranous sheath. As *V. cholerae* flagellins are not known to be glycosylated, and our structure does not reveal any densities consistent with glycosylation, the filament surface appears to be primarily composed of hydrophilic residues: threonine, serine, asparagine and aspartate (Fig. 3d,e). To explore the conservation of the sheet-and-helix motif, we used the Dali server[28] to search for structural homologues of the *V. cholerae* D2 domain. A top match was the outer domain from the *C. jejuni* major flagellin FlaA[29] (Extended Data Fig. 7). The residues in *C. jejuni* FlaA that correspond to the sheet-and-helix motif of *V. cholerae* FlaD are positioned alongside the outer surface of glycosylation sites, potentially shielding them from the surrounding milieu (Extended Data Fig. 7). Notably, the sheet-and-helix motif is not present in other well-studied flagellins, such as *P. aeruginosa*[27], *Escherichia coli*[30] and *S.* Typhimurium[15] (Extended Data Fig. 7).

FlaA serves as a template for filament assembly in *V. cholerae*

As FlaA is essential for flagellar filament assembly[11] and is mainly located at the beginning of the filament, where FlaD is less abundant (Fig. 1), we specifically selected the filament–hook junction area for cryo-EM data collection and analysis (Fig. 4a–f and Extended Data Fig. 8a–d). From 15,919 cryo-EM images near the proximal end of the flagellum, we determined a 3.43 Å structure of the filament–hook junction that enabled us to identify two layers of unique densities corresponding to 22 FlaA subunits between the hook–filament junction and FlaD filament and to build the FlaA model (Fig. 4c–f). The primary structural differences between FlaA and FlaD lie in the 267–276 region, where FlaA contains two additional residues, K275 and T276 (Fig. 4b–d and Extended Data Fig. 1). This region is a straight helix in FlaD (Fig. 3b), whereas it forms a long loop in FlaA (Fig. 4d and Supplementary Video 2). To further understand the role of FlaA, we deployed cryo-electron tomography (cryo-ET) to visualize the cell poles of a Δ*flhG*Δ*flaA* mutant (Extended Data Fig. 9). Similar to the previous negative staining EM results[11], we found short appendages at the poles of the Δ*flhG*Δ*flaA* mutant, which correspond to flagellar hooks ((Extended Data Fig. 9a). Their length was measured as ~55 nm, in agreement with values reported for *Salmonella*[31]. In some cases, however, we observed appendages extending up to ~100 nm (Extended Data Fig. 9b). In these tomograms, continuous filament-like densities were clearly visible beyond the hook, indicating that they represent filaments rather than elongated hooks. These findings suggest that filament assembly is reduced but not completely abolished in the absence of FlaA, and that FlaA functions as a template or adaptor to promote filament assembly by the other flagellins, FlaB–D.

FlaB structure at the filament tip

Our fluorescence microscopy data show that FlaB mainly localizes to the tip of the filament, where signals from other flagellins are very

https://doi.org/10.1038/s41564-025-02161-x

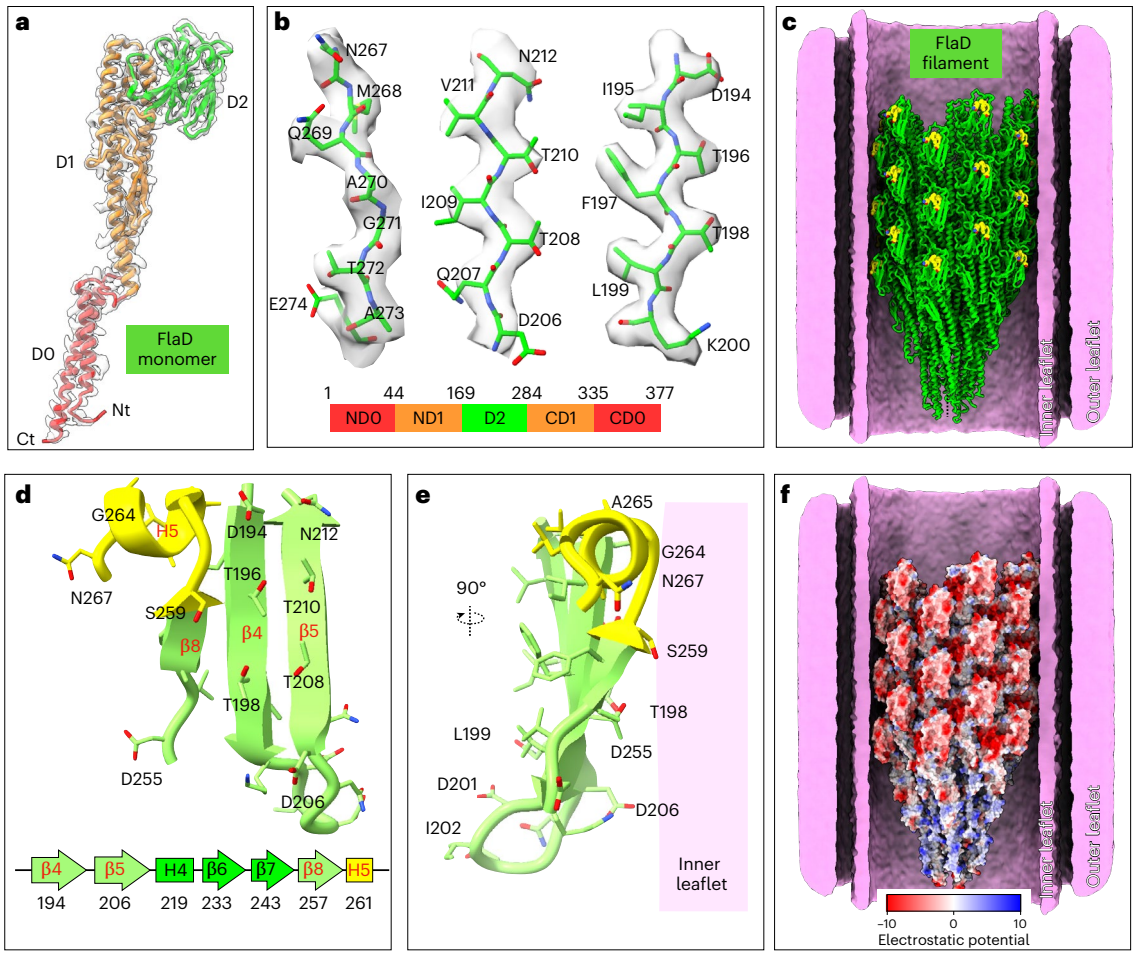

Fig. 3 | The sheathed flagellar filament in *V. cholerae* Δ*flhG* is predominantly formed by flagellin protein FlaD. a, Atomic model of FlaD fits well into one subunit of the cryo-EM map at 2.92 Å resolution. **b**, Three zoomed-in views in the D2 domain show the side-chain densities around residues 194–200, 206–212 and 267–274, respectively. **c**, FlaD model of the straight filament surrounded by the membranous sheath. Three-stranded β-sheet and H5 helix of flagellin FlaD are located on the filament surface adjacent to the membranous sheath. Residues 259–267 (H5) are coloured in yellow. **d**,**e**, Two close-up views of the three-stranded β-sheets (β4, β5 and β8) and helix motif (H5), which are positioned adjacent to the inner leaflet of the membranous sheath. **e** is rotated 90° counterclockwise relative to **d** to emphasize the interface between the filament and the inner leaflet of the outer membrane. **f**, The hydrophilic, negative-charged flagellar filament surface is adjacent to the inner leaflet of the membranous sheath (pink).

low (Fig. 1b,e). To determine a structure of FlaB, we manually selected 19,040 filament tips from 15,916 cryo-EM images and analysed the data separately (Fig. 4g–i and Extended Data Fig. 8e–h). Two-dimensional (2D) classes with well-defined membrane curvature at the tip were selected for filament structure determination at 3.16 Å resolution. Although the filament map lacks a cap structure, flagellin structures were sufficiently resolved to enable building a model of FlaB (Fig. 4i–l). Compared with other flagellins, such as FlaC and FlaD, FlaB lacks a residue at position 191, resulting in a total length of 376 amino acids (Extended Data Fig. 1). Despite variations in sequence, the D2 domain of FlaB exhibits a surface morphology consistent with that of FlaA and FlaD (Fig. 4k and Supplementary Video 3).

Cryo-EM structure of the FlaC filament

Although our fluorescence microscopy data clearly demonstrate that FlaC contributes to filament formation in wild-type *V. cholerae*, the fluorescence signal of FlaC appears considerably lower than that of FlaD, and both signals overlap at the middle of the filament, suggesting that FlaC is far less prominent than FlaD (Fig. 1c,e). Determination of a FlaC structure using the existing data from the Δ*flhG* mutant strain is thus impossible. To overcome this challenge, we constructed a Δ*flhG*Δ*flaBDE* mutant lacking three flagellins: FlaB, FlaD and FlaE. In the mutant cells, flagellar filaments are readily visible, although the number of flagella appears to be lower than in the parental Δ*flhG* strain (Extended Data Fig. 8i), indicating that FlaA and FlaC are sufficient for proper, although less efficient, flagellar filament assembly.

We then determined a cryo-EM structure of the flagellar filament in Δ*flhG*Δ*flaBDE* at 3.16 Å resolution (Extended Data Fig. 8i–l), enabling us to build a model of FlaC (Fig. 4m–r). Like the FlaD filament, the FlaC filament contains the sheet-and-helix motif on the surface. The residues in the β-sheets are highly conserved, differing only at residue S210 (T210 in FlaD). Unlike the mixture of serine, asparagine and glycine in FlaD, the helical motif in FlaC consists almost entirely of glycine residues (Fig. 4q). Nevertheless, the FlaC filament surface remains smooth and hydrophilic, as in other filaments (Figs. 3f and 4r and Extended Data Fig. 10). Taken together, our data indicate that FlaA serves as a template for filament assembly of FlaC as well as of other flagellin proteins.

Molecular architecture of the curved sheathed filament

Supercoiling of the bacterial flagellar filament of unsheathed flagella[14] is thought to be caused by 11 flagellin conformations. The flagellin structures in each protofilament resemble each other yet differ slightly between two adjacent protofilaments. However, it has remained unclear if similar mechanisms apply to sheathed flagella and how the filament interacts with the membranous sheath to enable supercoiling. To gain

https://doi.org/10.1038/s41564-025-02161-x

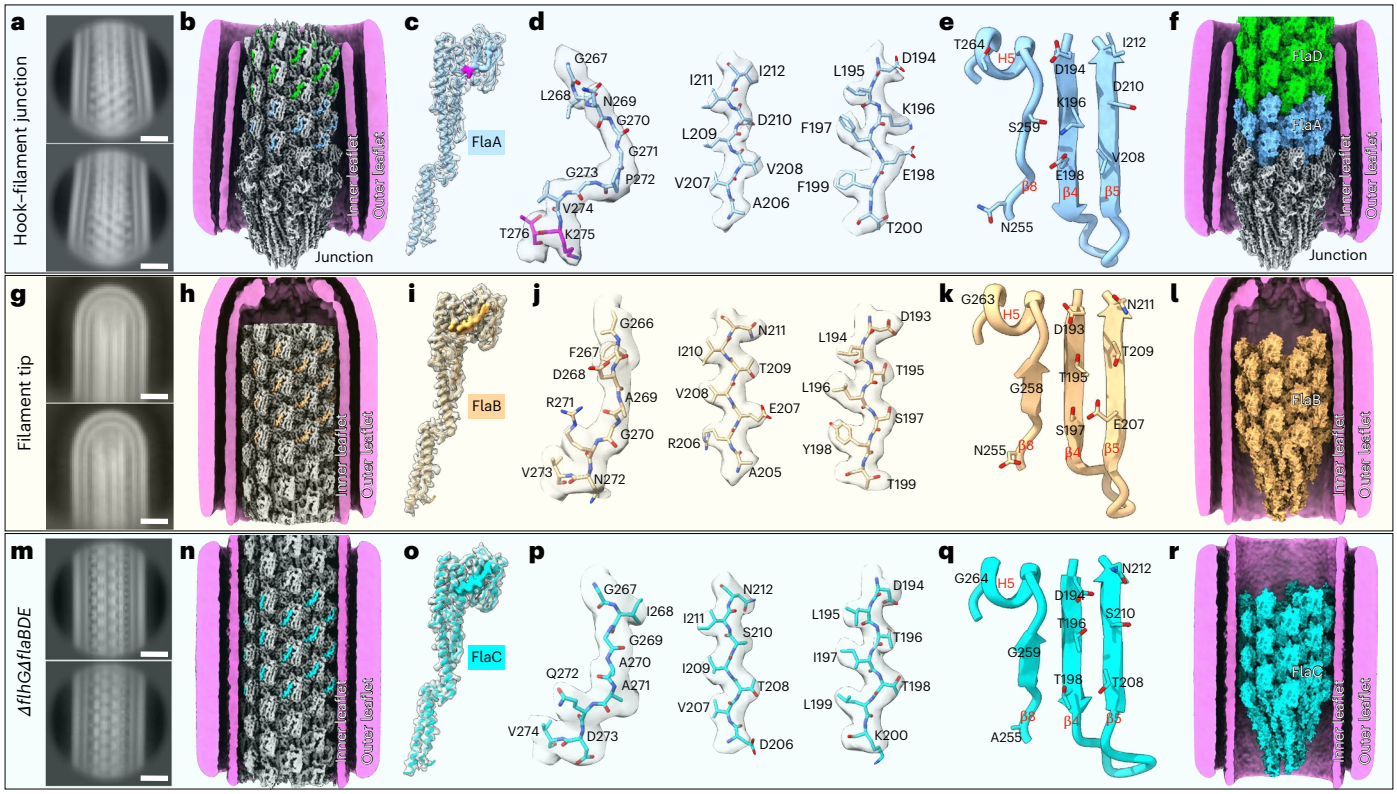

Fig. 4 | Flagellins FlaA–C across distinct filament regions. a, Two-dimensional class averages show the hook–filament junction. **b**, A surface view of a hook–filament junction structure at 3.43 Å resolution. The primary differences between FlaA and FlaD lie in the 267–276 region. The corresponding densities are coloured in green for FlaD and light blue for FlaA. **c**, The FlaA densities were identified based on the 267–276 densities and then used to build the FlaA model. Densities of K275–T276 are highlighted in magenta, which is absent in the other three flagellins. **d**, Side chains of three regions in 194–200, 206–212 and 267–276 fit well into the map. **e**, A close-up view of three-stranded β-sheets and one helical motif in FlaA. **f**, A model showing that 22 FlaA monomers (light blue) form a short adaptor bridging the FlaD filament (green) and junction (grey). **g**, Two-dimensional class averages showing the filament cap region. **h**, Cryo-EM structure of the filament close to the filament cap in Δ*flhG* mutant determined at 3.16 Å resolution. **i**, Atomic model of the FlaB monomer. **j**, Side-chain densities around residues 194–200, 206–212 and 267–274 in the D2 domain. **k**, A close-up view of three-stranded β-sheets (β4, β5 and β8) and one helical motif (H5) in FlaB. **l**, A model of the FlaB filament is surrounded by the membranous sheath (pink). **m**, Two-dimensional class averages of the sheathed flagella from Δ*flhG*Δ*flaBDE*. **n**, The 3.16 Å cryo-EM structure of the sheathed filament (cyan) from Δ*flhG*Δ*flaBDE* is surrounded by the membranous sheath (pink). **o**, The atomic model of FlaC fits well into one flagellin subunit map. **p**, Side-chain densities around residues 194–200 and 267–274 in the D2 domain are well visualized. Residue I197 in FlaC fits well into the Δ*flhG*Δ*flaBDE* density map. **q**, A close-up view of three-stranded β-sheets and one helical motif in FlaC. **r**, Atomic model of the FlaC filament surrounded by the membranous sheath.

mechanistic insights into supercoiling of the sheathed flagellum in *V. cholerae*, we utilized 2D and three-dimensional (3D) classification to determine a cryo-EM map of a highly curved filament (Fig. 5a and Extended Data Fig. 2). To understand how the protofilaments contribute to the curvature of the filament, we built a curved filament model (Fig. 5b) by aligning the backbone of flagellin FlaD and then comparing two distinct protofilaments with inner and outer curvature, each consisting of seven subunits (N_0, N_{11}, N_{22}, N_{33}, N_{44}, N_{55} and N_{66}), in the same curved filament (Fig. 5c,d). The protofilament length between subunits N_0 and N_{66} in the outer-curved conformation (322 Å) is considerably longer than in the inner-curved conformation (304 Å), consistent with prior results from unsheathed flagella[14]. Furthermore, the outer-curved protofilament is tilted 4° relative to the inner-curved protofilament, like the membranous sheath (Fig. 5c,d). With the D0 domain of the N_0 subunit in the inner-curved and outer-curved protofilaments aligned, the D1 domain shows a 3 Å shift in the inner curve compared with the outer curve (Fig. 5d). Intriguingly, the sheath-adjacent helical motifs of the 11 N_{66} subunits form a ring with a diameter of 59 Å, reflecting large conformational differences among the 11 protofilaments in the curved filament (Fig. 5e). These findings indicate that slight conformational changes at the single flagellin level can result in significant curvature in the protofilament. Importantly, the membranous sheath appears flexible enough to accommodate the curved filament.

Discussion

V. cholerae has evolved a remarkable ability to migrate to optimal niches, establish infection and evade host defences[10,32] through its unipolar sheathed flagellum. To better understand the sheathed flagellum and its unique adaptations, we have developed an innovative approach combining in situ cryo-EM with fluorescence microscopy and molecular genetics to characterize the sheathed flagellum from intact bacteria without flagella purification, which would otherwise disrupt the flagellum and surrounding membranous sheath. Critically, we reveal near-atomic structures of four flagellin proteins and their spatial distribution along the flagellar filament, providing mechanistic insights into the assembly and adaptation of the sheathed flagellum in *V. cholerae*.

First, although multiple flagellin genes are expressed in *V. cholerae*, each appears to play different roles in flagellar assembly. Our data indicate that FlaA is located at the hook–filament junction and plays a key role as a template for downstream filament assembly by other flagellin proteins (Fig. 4). FlaD is the major component of the filament, while FlaB is primarily located at the distal end. FlaC also contributes to filament assembly, although it is significantly less prominent than FlaD, at least in the Δ*flhG* mutant. Assembling a flagellum from multiple different spatially segregated flagellins improves motility in *Shewanella putrefaciens*[33] and may be similarly necessary for optimal swimming in *V. cholerae*. In addition, differential transcriptional[11]

https://doi.org/10.1038/s41564-025-02161-x

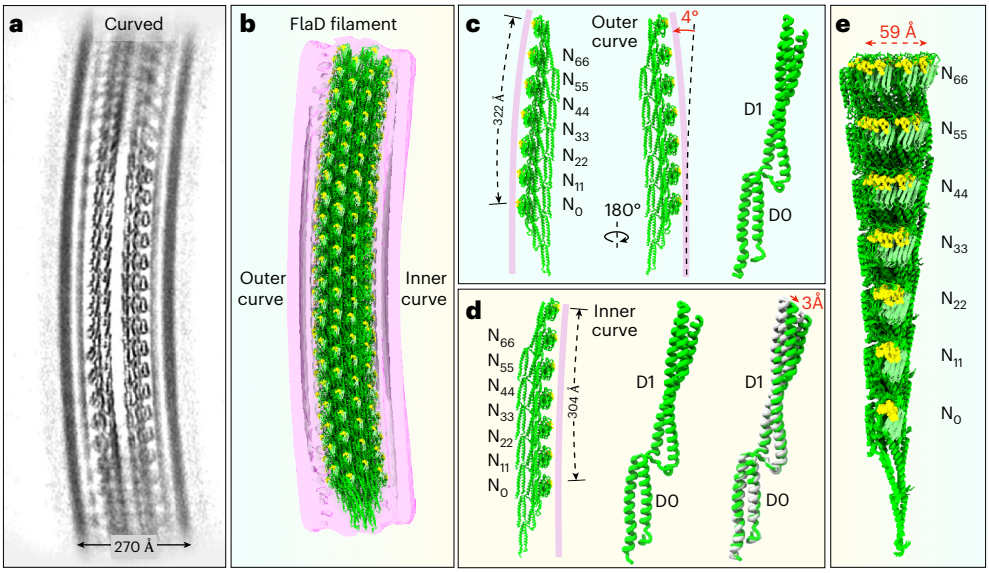

Fig. 5 | Cryo-EM structure of the curved sheathed filament reveals conformational changes in the flagellins, flagellar supercoiling and membranous curvature. a, A class average shows a curved sheathed filament and the membrane sheath with distinct inner and outer curves. **b**, The model of the curved FlaD filament shows β-sheets and helix motifs (yellow) on the surface of the curved filament. **c**, The model of the outer-curved protofilament. The total length of the seven-subunit protofilament is 322 Å. The filament surface is positioned adjacent to the inner leaflet (pink line) of the membranous sheath. The outer-curved protofilament is tilted by 4° from the inner-curved protofilament. A close-up view of the two domains of the flagellin FlaD (D0 and D1) are shown on the right. **d**, The model of the inner-curved protofilament. The total length of the seven-subunit protofilament is 304 Å. The inner-curved protofilament is slightly shorter than the outer-curved protofilament in **c**. Compared with the model from the flagellin in outer-curved protofilament, the top portion of the D1 domain undergoes a 3 Å shift while the D0 domain remains unchanged. **e**, Alignment of the 11 protofilaments shows the large conformational changes in the filament surface, resulting in a ~59 Å shift of the seven-subunit protofilament.

and posttranslational[34] controls over flagellin expression may allow *V. cholerae* to adapt its flagella to changing environmental conditions.

Second, although the sheathed flagellum in *V. cholerae* shares a conserved core and assembly mechanism with unsheathed flagella from other bacterial species[15,27,30], their filament surface features and overall size are strikingly different (Extended Data Fig. 4). We reveal that the flagellar filament surface in *V. cholerae* is largely formed by a distinct sheet-and-helix motif composed of amino acid residues such as serine, threonine and asparagine. Together, these form a relatively smooth and highly hydrophilic surface adjacent to the inner leaflet of the membranous sheath. As the membranous sheath consists of phospholipid in the inner leaflet and LPS in the outer leaflet, the overall diameter of the sheathed filament increases from 160 Å to 270 Å, or even further considering the long O-antigen and saccharide core of LPS. Therefore, the overall sheathed flagellar filament is significantly larger than any known unsheathed filaments, possibly allowing it to generate more thrust than a comparable unsheathed filament.

Lastly, specific interactions between the flagellar filament and surrounding membranous sheath are not evident in our filament structures, consistent with the model wherein the filament rotates independently of the sheath, causing it to rotate by propagating a spiral wave along the whole sheathed flagellum[19] (Supplementary Video 4). More experimental data, such as real-time lipid tracking, would be required to confirm this hypothesis.

In summary, we solved the near-atomic structure of the sheathed flagellar filament in intact *V. cholerae* cells, providing molecular insights into the assembly and adaptation of sheathed flagella as well as exposing a vulnerability in *V. cholerae* to the development of therapeutic strategies that inhibit motility and infection.

Methods

Strain construction

To fluorescently image each flagellin, strains JST124, JST190, JST366 and JST245 (Supplemental Data Table 1) were derived from wild-type *V. cholerae* O1 biovar El Tor strain C6706 by making two cysteine substitutions in the appropriate flagellin. These strains were inoculated into Luria–Bertani Miller (LB) medium from frozen stock and cultured aerobically at 30 °C overnight. To avoid LB autofluorescence, overnight cultures were diluted 1/30 in M9 minimal medium (Sigma-Aldrich) supplemented with 2 mM $MgSO_4$ (JT Baker), 100 µM $CaCl_2$ (JT Baker) and 0.5% glucose. Regrowth was performed aerobically at 37 °C to an optical density at a wavelength of 600 nm (OD_{600}) of 0.8–1.0.

The *flhG* deletion plasmid was constructed using Gibson Assembly (New England Biolabs) with primers *flhG*_delA, *flhG*_delB, *flhG*_delC and *flhG*_delD (Supplementary Table 2). Polymerase chain reaction (PCR) amplification was performed using Q5 High-Fidelity DNA Polymerase (New England Biolabs) following the instructions of the manufacturer, and the final construct was validated by DNA sequencing. Deletion of *flhG* was carried out as described[35]. The deletion plasmid was introduced into *V. cholerae* O1 El Tor A1552 via biparental mating using *E. coli* S17-1 λpir as the donor strain. Transconjugants were selected on LB agar supplemented with rifampicin (100 µg ml^{-1}) and ampicillin (100 µg ml^{-1}). Successful *flhG* deletion was confirmed by PCR using the primers *flhG*_delA and *flhG*_delD.

V. cholerae Δ*flaA* and Δ*flaEDB* flagellar mutants were generated in the O1 El Tor A1552 strain by allelic exchange using pKEK1989 and pKEK1854, as previously described[36]. A1552 Δ*flaA* Δ*flhG* and A1552 Δ*flaEDB* Δ*flhG* mutants were generated by chitin-induced natural transformation using the MuGENT technique[37]. The Δ*flhG* deletion was PCR amplified from KKV1701[23] with primers *flhG* + 3000 F and *flhG* + 3000 R (Supplementary Table 2), and the Δ*Vc1807*::CmR mutation was PCR amplified from TND0447 with primers ABD344 and ABD345[37]. The chromosomal Δ*flhG* mutations were verified by sequencing.

Bacterial culture

Δ*flhG* cells were cultivated aerobically at 30 °C with LB broth, which consisted of 1% tryptone, 0.5% yeast extract and 1% NaCl, adjusted to a pH of 7.5. Overnight cultures were prepared as follows: bacterial

strains were streaked from frozen glycerol stocks onto LB-agar plates and incubated at 30 °C overnight. Then five colonies were picked and inoculated into 5 ml of LB medium, then cultured overnight at 30 °C with shaking at 200 rpm. To initiate the experimental culture, a 1/200 dilution of the overnight culture was made in fresh LB medium, and the culture was grown until reaching an OD_{600} of 0.3–0.5.

Δ*flhG*Δ*flaA* and Δ*flhG*Δ*flaBDE* cells were cultured overnight on an LB plate containing 200 μg ml^{-1} streptomycin. A 1/200 dilution was then prepared in fresh LB medium supplemented with 200 μg ml^{-1} streptomycin and 2 μg ml^{-1} chloramphenicol, followed by incubation until the OD_{600} reached 0.3–0.5.

Construction of the strains for flagella labelling

Linear PCR products were constructed using splicing-by-overlap extension PCR as previously described and used as transforming DNA (tDNA) in chitin-dependent transformation reactions[37]. In brief, splicing-by-overlap extension PCR was performed by amplifying an upstream region of homology and a downstream region of homology. The desired mutations were incorporated into the primers used in amplification. All primers used to construct mutant alleles are listed in Supplementary Table 2. For chitin-dependent transformation, individual *V. cholerae* colonies were grown in LB medium at 30 °C for 6 h to an OD_{600} of 0.8–1.0. Cells were washed with Instant Ocean solution and then incubated with chitin particles suspended in Instant Ocean for 8–16 h at 30 °C before the tDNA was added. The cultures were then incubated at 30 °C for an additional 4–16 h. LB was added to the cultures and incubated at 37 °C for 2 h before plating on LB agar with the appropriate antibiotic. The desired mutants were selected by colony PCR screening. The location for introducing cysteine labelling has been described before in FlaA[22], and through homology with FlaA, we identified proper locations for labelling in FlaB, FlaC and FlaD.

Sample preparation for fluorescence imaging of the flagellins

Regrown cell culture was centrifuged at 4,000 rcf for 4 min, and the supernatant was removed and replaced with Alexa Fluor 488 C5-maleimide (Thermo Fisher Scientific) at a concentration of 25 μg ml^{-1} diluted in M9 minimal medium supplemented with 2 mM $MgSO_4$ and 100 μM $CaCl_2$ (hereafter M9 medium). Cells were resuspended by gentle pipetting using cut tips. This suspension was incubated at room temperature for 10 min before being washed three times by centrifuging cells as before, replacing supernatant with fresh M9 media and gently pipette mixing the cells to resuspend. A plate of 1.5% agarose prepared with M9 medium was sectioned into cubes with a razor blade to form agarose pads. One microlitre of fluorescently labelled cell suspension was added onto a coverglass, and an agarose pad was gently placed on top to trap the cells in a thin layer and prevent flagellar rotation during imaging. Thus prepared samples were imaged with a spinning disk confocal microscope (Nikon Ti2-E connected to Yokogawa W1) using a 100× silicone objective (numerical aperture 1.35) and captured with a sCMOS camera (Photometrics Prime BSI). Cells constitutively express mScarlet-I in the cytosol and were excited at 561 nm; the flagellar signal was captured with 488-nm laser excitation. Subsequently, 0.5 μl of membrane stain FM 1-43 at 5 mg ml^{-1} (Sigma-Aldrich) was added to the side of the agarose pad and allowed to diffuse to the cells and to stain the entire cell membrane including the flagellar sheath. The sample was subsequently imaged again in the 488 nm channel. Custom codes were subsequently developed to analyse the distribution of each flagellin along the flagellum. The origin of the flagella is determined by the fixed threshold in the cytosolic signal (mScarlet-I). Distance was calculated along curvilinear path of the flagella.

Preparation of cryo-EM samples

V. cholerae cells were centrifuged in 1.5-ml tubes at 2,348*g* for approximately 5 min, and the resulting pellet was gently rinsed with phosphate-buffered saline. The cell pellet was then resuspended in phosphate-buffered saline to a final OD_{600} of 1.0 to prepare the sample for plunge freezing.

Cryo-EM samples were prepared using copper grids with a holey carbon support film (200 mesh, R2/1, Quantifoil). The grids were glow-discharged for ~30 s before sample application. A 5-μl aliquot of the cell suspension was deposited onto each grid, which was subsequently blotted with filter paper (Whatman) for approximately 6 s. The grids were then rapidly plunged into a liquid ethane and propane mixture using a GP2 plunger (Leica). During the plunge-freezing process, the GP2 environmental chamber was maintained at 25 °C and 95% humidity to optimize sample vitrification.

In situ cryo-EM data collection and processing

Cryo-EM grids were imaged on a 300 kV Titan Krios electron microscope (Thermo Fisher Scientific), equipped with a field emission gun and a post-GIF K3 Summit Direct Electron Detector (Gatan). The nanoprobe settings for imaging were as follows: magnification of 81,000×, spot size of 5, illumination aperture (IA) of 1.22 μm and a slit width of 20 eV. The C2 aperture was set to 50 μm, and the objective aperture was set to 100 μm. A customized multishot script was used to directly image the cells on the cryo-EM grids using SerialEM[38], with defocus values ranging from 1.5 μm to 2.5 μm. The total dose applied during imaging was approximately 70 e^- Å^{-2}. The physical pixel rate was 32.5 e^- per pixel per second, and the effective pixel size was 1.068 Å per physical pixel (super-resolution mode, half of the physical pixel size). Each image exposure time was 2.46 s, divided into fractions of 0.0615 s per exposure. A total of 18,064 micrographs were collected from Δ*flhG* cells, and 755 micrographs were captured from Δ*flhG*Δ*flaBDE* cells (Supplementary Table 3).

All recorded images were initially motion-corrected[39] and then run Patch CTF Estimation[40] in cryoSPARC (Extended Data Fig. 2). The Manually Curate Exposures function was then used to select images with a relative ice thickness between 0.9 μm and 1.1 μm, a defocus tilt angle range of 0.1–22.7° and a defocus range of 76–10,067 Å. The Filament Tracer function[41] in cryoSPARC was used to pick 2D particles with the following parameters: filament diameter of 360 Å, minimum distance of 0.15 Å and minimum filament length of 1 Å. Multiple cycles of 2D classification were performed to isolate the particles of interest.

A total of 103,479 particles lacking the sheath were initially identified from 1,132,628 particles after 2D classification. These non-sheathed particle classes were used as a starting point for ab initio reconstruction, resulting in a low-resolution, non-symmetrical structure. Using this structure as an initial model, several iterative cycles of homogeneous and local refinement were performed, ultimately achieving a resolution of approximately 6 Å. The Symmetry Search Utility function in cryoSPARC[24] was then used to determine the helical parameters, including helical rise and helical twist. The top-ranked solution, with a helical rise of 4.74 Å and a twist of 65.41°, was selected. Using these parameters, the final helical reconstruction of the non-sheathed flagellar filament reached a near-atomic resolution of 2.45 Å (Extended Data Fig. 2e).

Subsequently, the same helical parameters of helical rise and helical twist were applied to the 2D-classified particles from the sheathed flagellar filament during helical refinement. Several iterative cycles of helical and local refinements were performed. Ultimately, the helical reconstruction map of the sheathed flagellar filament achieved a near-atomic resolution of 2.73 Å (Supplementary Table 3).

As previously described, an asymmetric approach for determining the structure of supercoiled flagellar filaments using cryo-EM was extensively applied. Specifically, this process involved starting with helical reconstruction and subsequently using a low-pass filtered version of the reconstruction (~20 Å) as the initial model[14,27,30]. The 2D classified particles were reprocessed from scratch, using a low-pass filtered volume as the initial reference. Homogeneous refinement was first applied, followed by local refinement of the filament core. During the local refinement, the rotation search range was gradually reduced

from the default 20° to 2°, and the shift search range was decreased from 10 Å to 2 Å. The initial low-pass filter was also progressively tightened from 12 Å to 3 Å. These refinements ultimately yielded asymmetric reconstructions of the sheathed FlaD filament at 2.92 Å resolution in Δ*flhG* cells (Extended Data Fig. 2) and the FlaC filament at 3.16 Å resolution in Δ*flhG*Δ*flaBDE* cells (Extended Data Fig. 8i–l).

Following this, through extensive 3D classification, 11,715 particles exhibited distinct curvature. These particles were selected and reconstructed at 3.61 Å resolution. To exhibit its curvature better, we reextracted the particles with 1,280 box size based on the curved flagellar filament structure from Δ*flhG* cells (Extended Data Fig. 2g)

To determine flagellin FlaA structure, we further acquired 15,919 cryo-EM micrographs from Δ*flhG V. cholerae* cells following the protocol described above (Extended Data Fig. 8a–d). Particles were manually selected, followed by the machine-learning-based algorithm Topaz[42] to identify particles across all micrographs. Ultimately, we selected 37,872 particles located in the hook–filament junction. Through homogeneous refinement, local refinement and helical refinement, we successfully determined the structure of FlaA flagellin at 3.43 Å resolution (Extended Data Fig. 8d).

To solve the flagellin FlaB structure, we manually selected 19,040 filament tip particles from 15,919 micrographs (Extended Data Fig. 8e–h). Following 2D classification, ab initio reconstruction was performed to generate initial models. Subsequent heterogeneous refinement enabled further 3D classification of conformational states. To align the tip structures for further refinement, we used the volume alignment tool in cryoSPARC to reorient each initial model into a vertical orientation. After aligning all particles vertically, the map centre was shifted just below the filament tip to focus refinement on the filament core. Particles were then reextracted using this new centre, and local refinement was carried out using a cylindrical soft mask. This workflow enabled structure determination of the FlaB filament at 3.16 Å resolution (Extended Data Fig. 8h).

Cryo-ET data collection and reconstruction of tomograms

Frozen-hydrated specimens of Δ*flhG*Δ*flaA* cells were imaged using a 300 kV Titan Krios electron microscope (Thermo Fisher Scientific) equipped with a field emission gun and a K3 Summit post-GIF Direct Electron Detector (Gatan). Tilt series were collected using SerialEM[38] and the FASTTOMO script[43], following the dose-symmetric method. The defocus was set to −4.8 µm, with a total electron dose of approximately 70 e^{-} $Å^{-2}$ distributed across 33 tilt images spanning angles from −48° to 48° in 3° increments. Motion correction of the recorded images was performed using MotionCorr2[39] and then stacked and aligned by using IMOD[44]. The 6× binned tomograms were then reconstructed by using Tomo3D[45]. In total, we generated 22 reconstructions from Δ*flhG*Δ*flaA* cells.

Modelling

Amino acid sequences of FlaA to FlaE were obtained from UniProt (accession numbers P0C6C3 to P0C6C7) and used as input for AlphaFold3[46] to generate predicted structural models of the flagellin monomers. The predicted models were fitted into the cryo-EM map using ChimeraX[47], followed by real-space refinement in Phenix[48] and Coot[49]. The final monomer models demonstrated excellent stereochemistry, as assessed by Phenix. Furthermore, Phenix reported map-to-model correlation coefficients of 0.83, 0.84, 0.84 and 0.86 for FlaA, FlaB, FlaC and FlaD, respectively. These correlation coefficients served as robust cross-validation metrics for evaluating map quality and helical symmetry parameters. Furthermore, the residue region 267–276 extends beyond the cryo-EM density, indicating poor model-to-map fit. Additional discrepancies were observed in FlaB and FlaC, where several residues do not align well with the cryo-EM densities (Extended Data Fig. 3).

Using the FlaD monomer, we modelled the helical flagellar filament in Phenix by fitting 33 subunits of FlaD into the helical cryo-EM density map. A similar strategy was applied to the asymmetrical density maps of flagellar filaments to assess the flagellin network. We aligned the backbone of the FlaD model to the curved density at 3.61 Å resolution.

In Δ*flhG*Δ*flaBDE* cells, both FlaA and FlaC models were fitted into the cryo-EM density map in Phenix[48], with FlaC exhibiting a closer fit. Therefore, the FlaC model was constructed for Δ*flhG*Δ*flaBDE* cells.

The AlphaFold3[46]-predicted models of FlaA and FlaB were fitted into corresponding cryo-EM density maps by ChimeraX[47], followed by real-space refinement in Phenix[48] and Coot[49].

All sequence alignments in this study were performed using Clustal Omega alignment[50] and the Dali server[28]. UCSF ChimeraX[47] was utilized for surface rendering of cryo-EM density maps and segmentation. All the structures were validated in Phenix[48] using the Phenix Map validation tool, and the map quality was assessed using the Mtriage tool in Phenix[48], as reported in Supplementary Table 5.

Reporting summary

Further information on research design is available in the Nature Portfolio Reporting Summary linked to this article.

Data availability

The atomic coordinates and corresponding density maps of the flagellins have been deposited in the Protein Data Bank (PDB) and the Electron Microscopy Data Bank (EMDB). The FlaA filament from the Δ*flhG V. cholerae* strain is available via PDB at 9N8G and EMD-49128. The FlaB filament from the same strain is available via PDB at 9P7R and EMD-71351. The FlaC filament from the Δ*flhG*Δ*flaBDE* strain is available via PDB at 9N8M and EMD-49131. The FlaD filament from the Δ*flhG* strain is available via PDB at 9N8A and EMD-49125 (Supplementary Table 3).

References

1. Bartlett, T. M. et al. A periplasmic polymer curves *Vibrio cholerae* and promotes pathogenesis. *Cell* **168**, 172–185 e115 (2017).
2. Colwell, R. R. Global climate and infectious disease: the cholera paradigm. *Science* **274**, 2025–2031 (1996).
3. Reidl, J. & Klose, K. E. *Vibrio cholerae* and cholera: out of the water and into the host. *FEMS Microbiol. Rev.* **26**, 125–139 (2002).
4. Ali, M., Nelson, A. R., Lopez, A. L. & Sack, D. A. Updated global burden of cholera in endemic countries. *PLoS Negl. Trop. Dis.* **9**, e0003832 (2015).
5. Conner, J. G., Teschler, J. K., Jones, C. J. & Yildiz, F. H. Staying alive: *Vibrio cholerae*'s cycle of environmental survival, transmission, and dissemination. *Microbiol. Spectr.* https://doi.org/10.1128/microbiolspec.VMBF-0015-2015 (2016).
6. Almagro-Moreno, S., Pruss, K. & Taylor, R. K. Intestinal colonization dynamics of *Vibrio cholerae*. *PLoS Pathog.* **11**, e1004787 (2015).
7. Wang, Z., Lazinski, D. W. & Camilli, A. Immunity provided by an outer membrane vesicle cholera vaccine is due to o-antigen-specific antibodies inhibiting bacterial motility. *Infect. Immun.* https://doi.org/10.1128/IAI.00626-16 (2017).
8. Montero, D. A. et al. *Vibrio cholerae*, classification, pathogenesis, immune response, and trends in vaccine development. *Front. Med.* **10**, 1155751 (2023).
9. Magariyama, Y. et al. Very fast flagellar rotation. *Nature* **371**, 752 (1994).
10. Grognot, M., Mittal, A., Mah'moud, M. & Taute, K. M. *Vibrio cholerae* motility in aquatic and mucus-mimicking environments. *Appl. Environ. Microbiol.* **87**, e0129321 (2021).
11. Klose, K. E. & Mekalanos, J. J. Differential regulation of multiple flagellins in *Vibrio cholerae*. *J. Bacteriol.* **180**, 303–316 (1998).
12. Yoon, S. S. & Mekalanos, J. J. Decreased potency of the *Vibrio cholerae* sheathed flagellum to trigger host innate immunity. *Infect. Immun.* **76**, 1282–1288 (2008).

13. Jung, Y. C., Lee, M. A. & Lee, K. H. Role of Flagellin-homologous proteins in biofilm formation by pathogenic *Vibrio* species. *mBio* https://doi.org/10.1128/mBio.01793-19 (2019).
14. Kreutzberger, M. A. B. et al. Convergent evolution in the supercoiling of prokaryotic flagellar filaments. *Cell* https://doi.org/10.1016/j.cell.2022.08.009 (2022).
15. Yamaguchi, T. et al. Structural and functional comparison of *Salmonella* flagellar filaments composed of FljB and FliC. *Biomolecules* https://doi.org/10.3390/biom10020246 (2020).
16. Blum, T. B., Filippidou, S., Fatton, M., Junier, P. & Abrahams, J. P. The wild-type flagellar filament of the Firmicute *Kurthia* at 2.8 Å resolution in vivo. *Sci. Rep.* **9**, 14948 (2019).
17. Wang, F. et al. A structural model of flagellar filament switching across multiple bacterial species. *Nat. Commun.* **8**, 960 (2017).
18. Chu, J., Liu, J. & Hoover, T. R. Phylogenetic distribution, ultrastructure, and function of bacterial flagellar sheaths. *Biomolecules* https://doi.org/10.3390/biom10030363 (2020).
19. Fuerst, J. A. Bacterial sheathed flagella and the rotary motor model for the mechanism of bacterial motility. *J. Theor. Biol.* **84**, 761–774 (1980).
20. Zheng, W., Chai, P., Zhu, J. & Zhang, K. High-resolution in situ structures of mammalian respiratory supercomplexes. *Nature* **631**, 232–239 (2024).
21. Drobnic, T. et al. In situ structure of a bacterial flagellar motor at subnanometre resolution reveals adaptations for increased torque. *Nat. Microbiol.* **10**, 1723–1740 (2025).
22. Zhang, W. et al. Crash landing of *Vibrio cholerae* by MSHA pili-assisted braking and anchoring in a viscoelastic environment. *eLife* https://doi.org/10.7554/eLife.60655 (2021).
23. Correa, N. E., Peng, F. & Klose, K. E. Roles of the regulatory proteins FlhF and FlhG in the *Vibrio cholerae* flagellar transcription hierarchy. *J. Bacteriol.* **187**, 6324–6332 (2005).
24. Punjani, A., Rubinstein, J. L., Fleet, D. J. & Brubaker, M. A. cryoSPARC: algorithms for rapid unsupervised cryo-EM structure determination. *Nat. Methods* **14**, 290–296 (2017).
25. Chatterjee, S. N. & Chaudhuri, K. Lipopolysaccharides of *Vibrio cholerae*. I. Physical and chemical characterization. *Biochim. Biophys. Acta* **1639**, 65–79 (2003).
26. Zhu, S. et al. Molecular architecture of the sheathed polar flagellum in *Vibrio alginolyticus*. *Proc. Natl Acad. Sci. USA* **114**, 10966–10971 (2017).
27. Nedeljkovic, M. et al. An unbroken network of interactions connecting flagellin domains is required for motility in viscous environments. *PLoS Pathog.* **19**, e1010979 (2023).
28. Holm, L. Dali server: structural unification of protein families. *Nucleic Acids Res.* **50**, W210–w215 (2022).
29. Kreutzberger, M. A. B., Ewing, C., Poly, F., Wang, F. & Egelman, E. H. Atomic structure of the *Campylobacter jejuni* flagellar filament reveals how epsilon Proteobacteria escaped Toll-like receptor 5 surveillance. *Proc. Natl Acad. Sci. USA* **117**, 16985–16991 (2020).
30. Kreutzberger, M. A. B. et al. Flagellin outer domain dimerization modulates motility in pathogenic and soil bacteria from viscous environments. *Nat. Commun.* **13**, 1422 (2022).
31. Erhardt, M., Singer, H. M., Wee, D. H., Keener, J. P. & Hughes, K. T. An infrequent molecular ruler controls flagellar hook length in *Salmonella enterica*. *EMBO J.* **30**, 2948–2961 (2011).
32. Silva, A. J. & Benitez, J. A. *Vibrio cholerae* biofilms and cholera pathogenesis. *PLoS Negl. Trop. Dis.* **10**, e0004330 (2016).
33. Kuhn, M. J. et al. Spatial arrangement of several flagellins within bacterial flagella improves motility in different environments. *Nat. Commun.* **9**, 5369 (2018).
34. Ghandour, R. et al. ProQ-associated small RNAs control motility in *Vibrio cholerae*. *Nucleic Acids Res.* https://doi.org/10.1093/nar/gkae1283 (2024).
35. Lim, B., Beyhan, S., Meir, J. & Yildiz, F. H. Cyclic-diGMP signal transduction systems in *Vibrio cholerae*: modulation of rugosity and biofilm formation. *Mol. Microbiol.* **60**, 331–348 (2006).
36. Echazarreta Mylea, A., Kepple Johnathan, L., Yen, L.-H., Chen, Y. & Klose Karl, E. A Critical region in the FlaA flagellin facilitates filament formation of the *Vibrio cholerae* flagellum. *J. Bacteriol.* https://doi.org/10.1128/jb.00029-18 (2018).
37. Dalia, A. B., McDonough, E. & Camilli, A. Multiplex genome editing by natural transformation. *Proc. Natl Acad. Sci. USA* **111**, 8937–8942 (2014).
38. Mastronarde, D. N. Automated electron microscope tomography using robust prediction of specimen movements. *J. Struct. Biol.* **152**, 36–51 (2005).
39. Zheng, S. Q. et al. MotionCor2: anisotropic correction of beam-induced motion for improved cryo-electron microscopy. *Nat. Methods* **14**, 331–332 (2017).
40. Noble, A. J. et al. Routine single particle CryoEM sample and grid characterization by tomography. *eLife* https://doi.org/10.7554/eLife.34257 (2018).
41. Huber, S. T., Kuhm, T. & Sachse, C. Automated tracing of helical assemblies from electron cryo-micrographs. *J. Struct. Biol.* **202**, 1–12 (2018).
42. Bepler, T. et al. Positive-unlabeled convolutional neural networks for particle picking in cryo-electron micrographs. *Nat. Methods* **16**, 1153–1160 (2019).
43. Xu, A. & Xu, C. FastTomo: a SerialEM script for collecting electron tomography data. Preprint at *bioRxiv* https://doi.org/10.1101/2021.03.16.435675 (2021).
44. Kremer, J. R., Mastronarde, D. N. & McIntosh, J. R. Computer visualization of three-dimensional image data using IMOD. *J. Struct. Biol.* **116**, 71–76 (1996).
45. Agulleiro, J.-I. & Fernandez, J.-J. Tomo3D 2.0—exploitation of Advanced Vector eXtensions (AVX) for 3D reconstruction. *J. Struct. Biol.* **189**, 147–152 (2015).
46. Abramson, J. et al. Accurate structure prediction of biomolecular interactions with AlphaFold 3. *Nature* **630**, 493–500 (2024).
47. Goddard, T. D. et al. UCSF ChimeraX: meeting modern challenges in visualization and analysis. *Protein Sci.* **27**, 14–25 (2018).
48. Liebschner, D. et al. Macromolecular structure determination using X-rays, neutrons and electrons: recent developments in Phenix. *Acta Crystallogr. D* **75**, 861–877 (2019).
49. Emsley, P. & Cowtan, K. Coot: model-building tools for molecular graphics. *Acta Crystallogr. D* **60**, 2126–2132 (2004).
50. Sievers, F. & Higgins, D. G. Clustal Omega for making accurate alignments of many protein sequences. *Protein Sci.* **27**, 135–145 (2018).

Acknowledgements

We thank J. Aronson for critical reading and editing of the paper. We thank C. Sindelar from Yale Center for Research Computing for providing support on cryo-EM data processing. W.G., J. Yue, J.W., J.G., J.M.B, R.K. and J.L. were partly supported by grants R01AI189907, R01AI087946 and R01AI132818 from the National Institute of Allergy and Infectious Diseases (NIAID) and National Institutes of Health (NIH). J.H.P. and F.H.Y. were supported by grants R01AI189907 and R01AI102584 from NIAID. V.S., H.H. and K.E.K. were supported by the Kleberg Foundation, Brown Foundation and San Antonio Area Foundation. J. Yan acknowledges the support from the National Science Foundation (MCB #2438891) and Simons Foundation International (SFI-LS-ECIAMEE-00006634). M.A. acknowledges the support from Charles H. Revson Foundation (25-19). J.-S.B.T. acknowledges the support from the Damon Runyon Cancer Research Foundation (DRG-2446-21). Cryo-EM data were collected at the Yale CryoEM Resource funded in part by NIH grant 1S10OD023603-01A1.

Author contributions

W.G. and J.L. conceived of the study. W.G. performed cryo-EM and cryo-ET data collection and processing. S.Z. initiated cryo-EM data processing of the non-sheathed flagellar filament structure. J.H.P. constructed the Δ*flhG* strain. V.S. and H.H. constructed the Δ*flhG*Δ*flaBDE* and Δ*flhG*Δ*flaA* strains for FlaC structural determination. M.A. and J.-S.B.T. performed flagellar labelling and fluorescence imaging of flagellins. J. Yue, J.W. and R.K. contributed to modelling, and J.G. contributed to manual picking of the flagellar tips and processing of the FlaB structure. J.M.B. produced the animation. S.W. assisted with data collection. J. Yan, K.E.K., F.H.Y. and J.L. provided critical resources, technical advice and supervision. W.G. and J.L. interpreted the data and wrote the paper with input from all authors. All authors discussed the results and approved the final version of the paper.

Competing interests

The authors declare no competing interests.

Additional information

Extended data is available for this paper at https://doi.org/10.1038/s41564-025-02161-x.

Supplementary information The online version contains supplementary material available at https://doi.org/10.1038/s41564-025-02161-x.

Correspondence and requests for materials should be addressed to Wangbiao Guo or Jun Liu.

Peer review information *Nature Microbiology* thanks Tina Iverson, Mohammed Kaplan and the other, anonymous, reviewer(s) for their contribution to the peer review of this work. Peer reviewer reports are available.

https://doi.org/10.1038/s41564-025-02161-x

```
FlaA  MTINVNTNVSAMTAQRYLTKATGELNTSMERLSSGNRINSAKDDAAGLQISNRLTAQSRG  60
FlaB  MAINVNTNVSAMTAQRYLNGAADGMQKSMERLSSGYKINSARDDAAGLQISNRLTSQSRG  60
FlaC  MAVNVNTNVSAMTAQRYLTSATNAQQSSMERLSSGYKINSAKDDAAGLQISNRLNVQSRG  60
FlaD  MAVNVNTNVAAMTAQRYLTGATNAQQTSMERLSSGFKINSAKDDAAGLQISNRLNVQSRG  60

FlaA  LDVAMRNANDGISIAQTAEGAMNESTSILQRMRDLALQSANGTNSASERQALNEESVALQ  120
FlaB  LDMAVKNANDGISIAQTAEGAMNETTNILQRMRDLALQSSNGSNSSSERRAIQEEVSALN  120
FlaC  LGVAVRNANDGISMAQTAEGAMKETTNILQRMRDLSLQSANGSNSKADRVAIQEEITALN  120
FlaD  LDVAVRNANDGISIAQTAEGAMNETTNILQRMRDLSLQSANGSNSKSERVAIQEEITALN  120

FlaA  DELNRIAETTSFGGRKLLNGSFGEASFQIGSSSGEAIIMGLTSVRADDFRMGGQSFIAEQ  180
FlaB  DELNRIAETTSFGGNKLLNGSFGSKSFQIGADSGEAVMLSMGSMRSDTQAMGGKSYRAQE  180
FlaC  DELNRVAETTSFGGNKLLNGTFATKSFQIGADNGEAVMLNIKDMRSDNALMGGKTYQAAN  180
FlaD  DELNRIAETTSFGGNKLLNGTFSTKSFQIGADNGEAVMLTLKDMRSDNRMMGGTSYVAAE  180

FlaA  PKTKEWGVPPTARDLKFEFTKKDGEAVVLDIIAKDGDDIEELATYINGQTDLFKASVDQE  240
FlaB  GKAADWRVGA-ATDLTLSYTNKQGEAREVTINAKQGDDLEELATYINGQTEDVKASVGED  239
FlaC  GKDKNWGVEAGKTDLTITLKDKREGDVTISINAKEGDDIEELATYINGQTDMIKASVDEE  240
FlaD  GKDKDWKVQAGANDITFTLKDIDGNDQTITVNAKEGDDIEEVATYINGQTDMVKASVNEK  240

FlaA  GKLQIFVAEPNIEGNFNISGGLATELGLNGGPGVKTTVQDIDITSVGGSQNAVGIIDAAL  300
FlaB  GKLQLFASSQKVNGDVTIGGGLGGEIGFDAGRNV--TVADVNVSTVAGSQEAVSILDGAL  297
FlaC  GKLQLFTDNNRIDGAATFGGALAGELGIGAAQDV--TVDTLDVTTVGGAQESVAIVDAAL  298
FlaD  GQLQIFAGNNKVTGDVAFSGGLAGALNMQAGTAE--TVDTIDVTSVGGAQQSVAVIDSAL  298

FlaA  KYVDSQRADLGAKQNRLSHSISNLSNIQENVEASKSRIKDTDFAKETTQLTKSQILQQAG  360
FlaB  KAVDSQRASLGAFQNRFGHAISNLDNVNENVNASRSRIRDTDYARETTAMTKAQILQQAS  357
FlaC  KYVDSHRAELGAFQNRFNHAINNLDNINENVNASKSRIKDTDFAKETTALTKAQILSQAS  358
FlaD  KYVDSHRAELGAFQNRFNHAISNLDNINENVNASKSRIKDTDFAKETTALTKSQILSQAS  358

FlaA  TSILAQAKQLPNSAISLLQ-  379
FlaB  TSVLAQAKQSPSAALSLLG-  376
FlaC  SSVLAQAKQAPNSALALLG-  377
FlaD  SSVLAQAKQAPNAALSLLG-  377
```

Extended Data Fig. 1 | Multiple sequence alignment of flagellins FlaA-D. Note that residues (259-267) are highlighted in blue. Residues (268-274, red) in FlaA exhibit a distinct morphology compared to other flagellins (FlaB, FlaC, and FlaD) due to two extra residues (K275 and T276, magenta).

https://doi.org/10.1038/s41564-025-02161-x

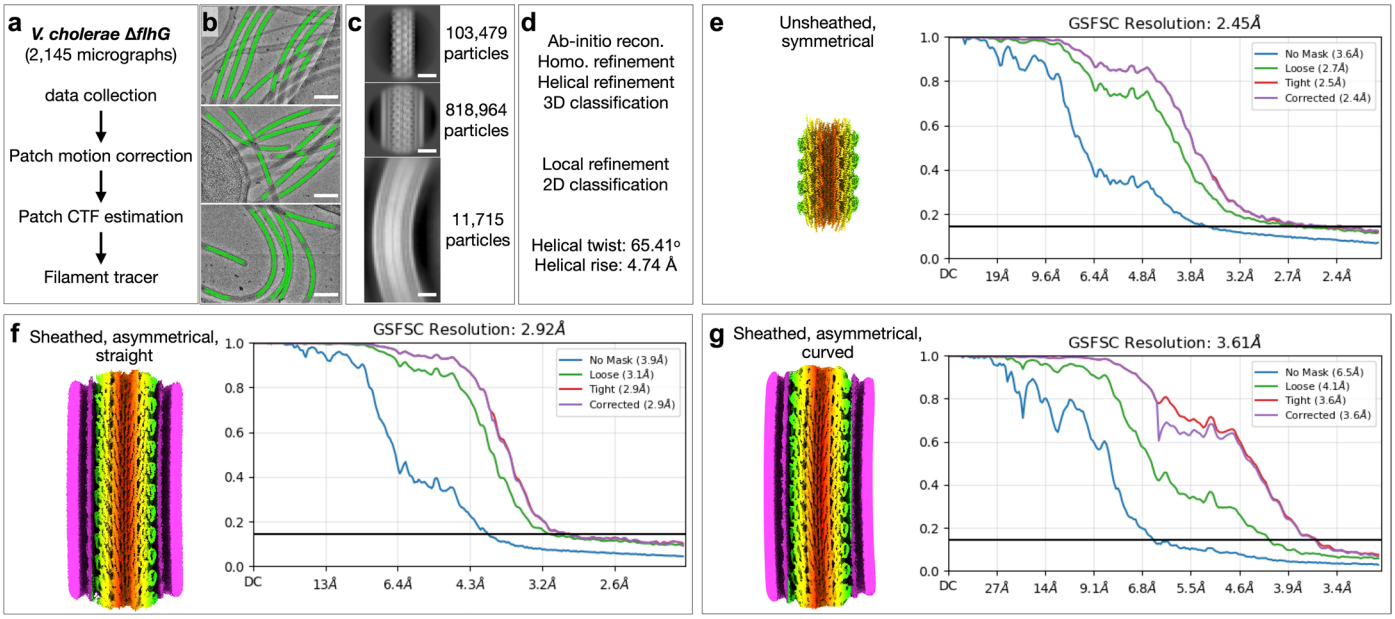

Extended Data Fig. 2 | CryoSPARC workflow for structural determination of the FlaD filament in *V. cholerae*. **(a)** A total of 2,145 micrographs were collected using a Titan Krios and processed in CryoSPARC. **(b)** Snapshots of filament tracer during particle picking. The representative images were acquired independently at least three times. Scale bar: 100 nm. **(c)** Representative 2D classifications showing unsheathed, sheathed, and curved flagellar filaments of Δ*flhG V. cholerae*. Scale bar: 200 Å. **(d)** Workflow of 3D reconstruction in CryoSPARC. *Ab initio* reconstruction was used to generate initial models, followed by homogeneous, helical, and local refinements to determine the helical twist and rise parameters. **(e)** Cryo-EM density map of the unsheathed flagellar filament after helical refinement, resolved at 2.45 Å based on the "gold standard" 0.143 FSC plot. **(f)** Cryo-EM density map of a sheathed, straight flagellar filament determined by homogeneous and local refinements without helical refinement, resolved at 2.92 Å. **(g)** Cryo-EM density map of a sheathed, curved flagellar filament resolved at 3.61 Å through homogeneous and local refinements without helical refinement.

https://doi.org/10.1038/s41564-025-02161-x

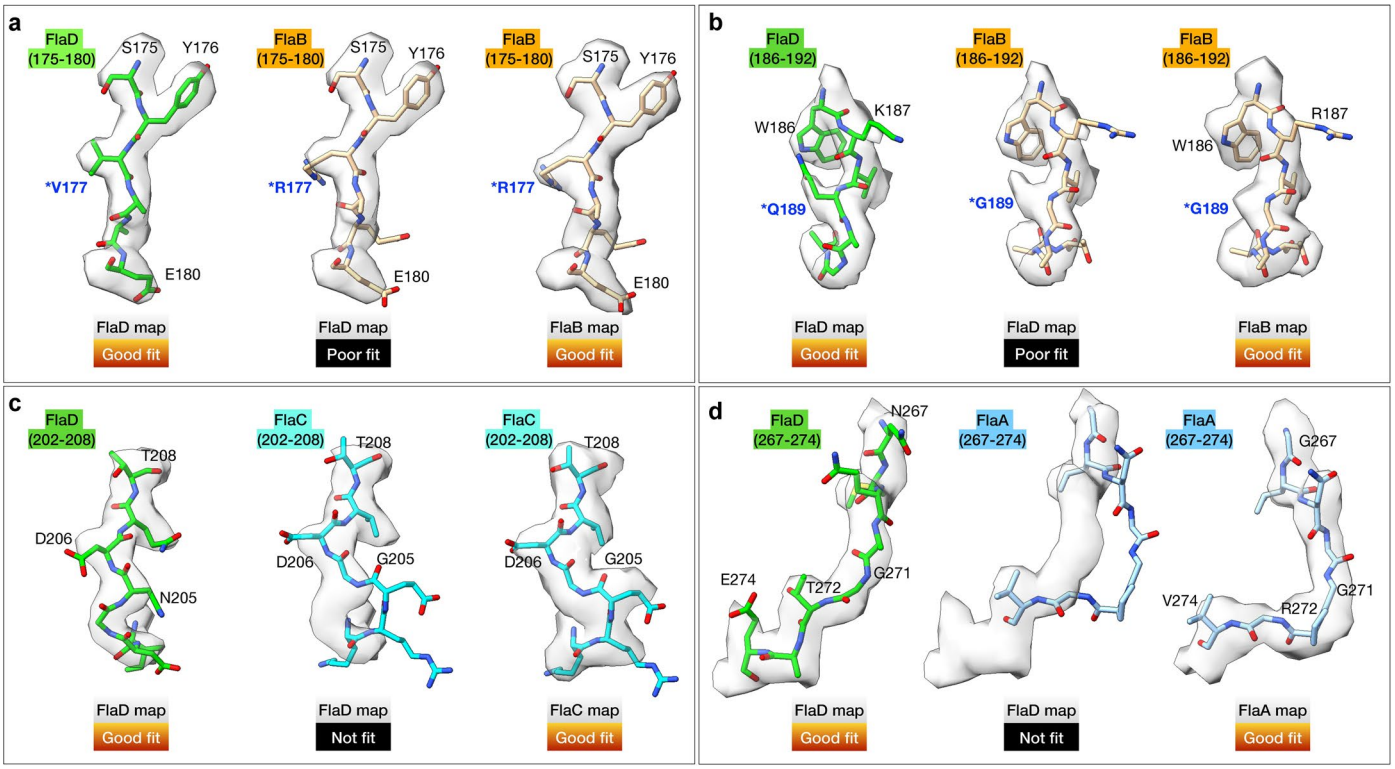

Extended Data Fig. 3 | Cryo-EM maps at near-atomic resolution enable structure determination of four flagellins (FlaA, FlaB, FlaC, and FlaD) in *V. cholerae*. (**a-d**) Representative model-to-map fits of FlaA, FlaB, FlaC, and FlaD into our cryo-EM maps derived from the *in-situ* cryo-EM map. Notably, the FlaD model fits well into the FlaD densities (left panels in **a-d**), while other models, including FlaA, FlaB, and FlaC, fit poorly into the FlaD densities (middle panels in **a-d**). The models of FlaA, FlaB, and FlaC fit well into their corresponding densities (right panels in **a-d**).

https://doi.org/10.1038/s41564-025-02161-x

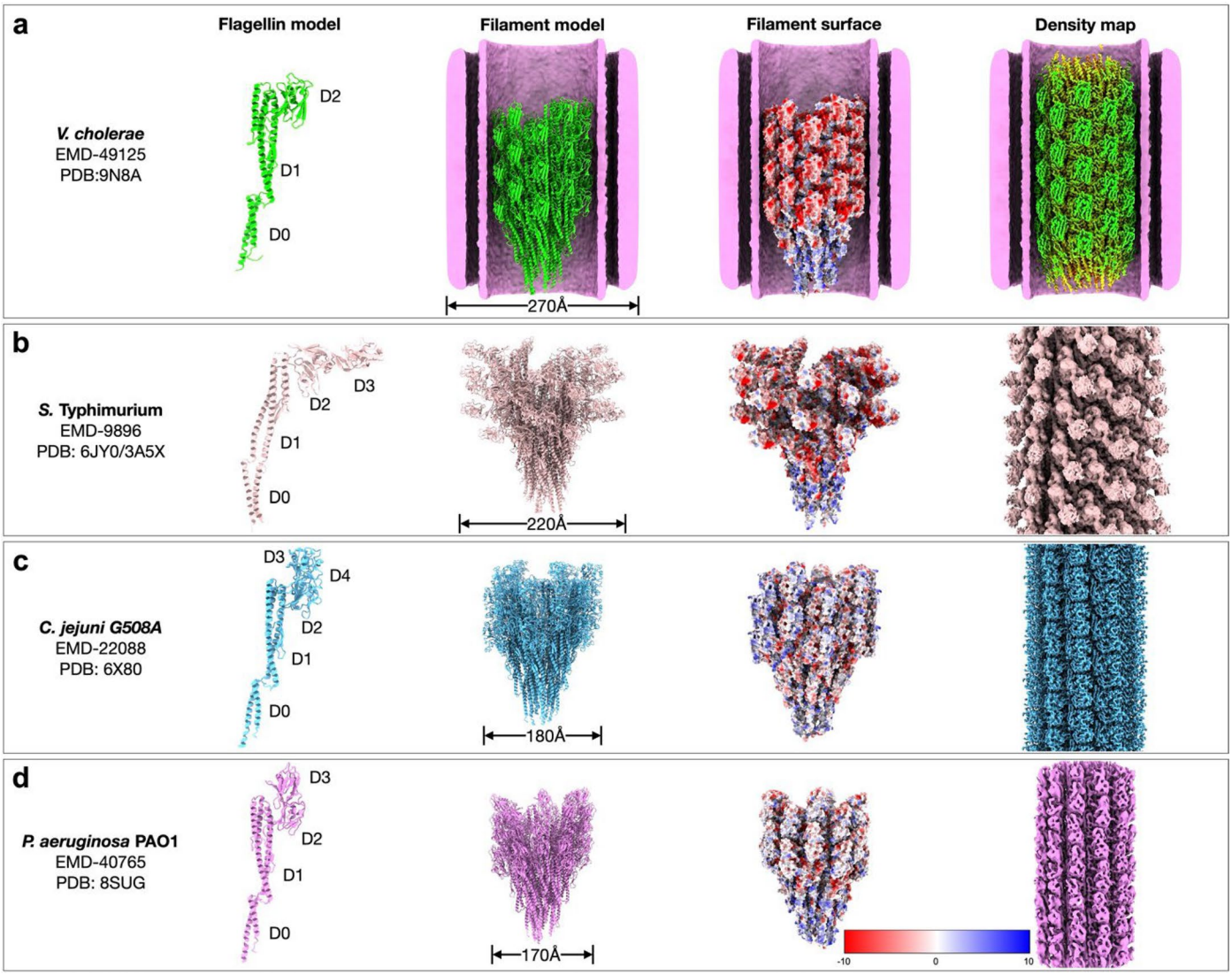

Extended Data Fig. 4 | Comparison of flagellar filament structures across bacterial species. (**a**) The flagellin model, filament model, surface electrostatic potential, and cryo-EM map from *V. cholerae* flagella are presented sequentially, left to right. The overall diameter of the sheathed filament is 270 Å. (**b**) The flagellin model, filament model, surface electrostatic potential, and cryo-EM map from *S.* Typhimurium[15] flagella are presented sequentially, left to right. The overall diameter of the filament is 220 Å. (**c**) The flagellin model, filament model, surface electrostatic potential, and cryo-EM map from *C. jejuni*[29] flagella are presented sequentially, left to right. The overall diameter of the filament is 180 Å. (**d**) The flagellin model, filament model, surface electrostatic potential, and cryo-EM map from *P. aeruginosa*[27] flagella are presented sequentially, left to right. The overall diameter of the filament is 170 Å.

https://doi.org/10.1038/s41564-025-02161-x

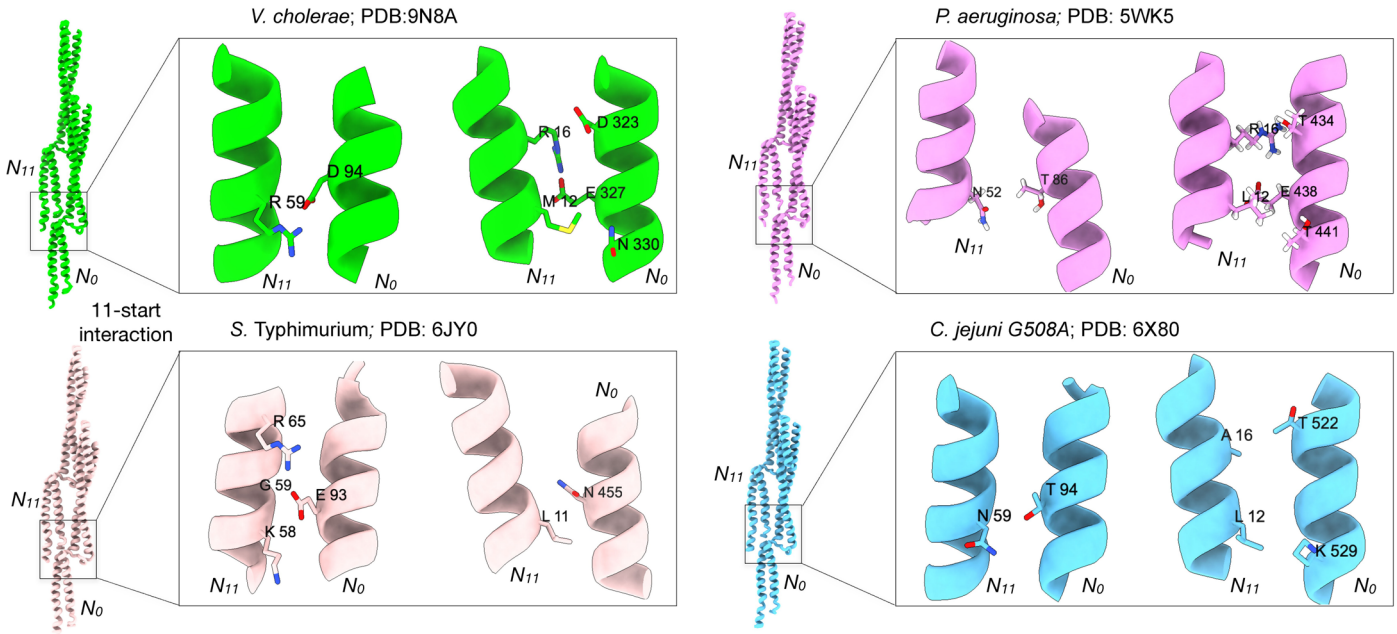

Extended Data Fig. 5 | Interdomain interactions along the 11-start interface across bacterial species. Three potential interaction pairs are: $D94_0$-$R59_{11}$, $D323_0$-$R16_{11}$, and $N330_0$-$M12_{11}$. Similar interactions are observed in other bacterial species, such as *S.* Typhimurium[15] ($E93_0$ and $G59_{11}$ or $K58_{11}$, $N455_0$ and $L11_{11}$), *P. aeruginosa*[27] ($T86_0$ and $N52_{11}$, $T434_0$ and $R16_{11}$, $E438_0$ and L1211), and *C. jejuni*[29] ($T94_0$ and $N59_{11}$, $T522_0$ and $A16_{11}$, $K529_0$ and $L12_{11}$).

https://doi.org/10.1038/s41564-025-02161-x

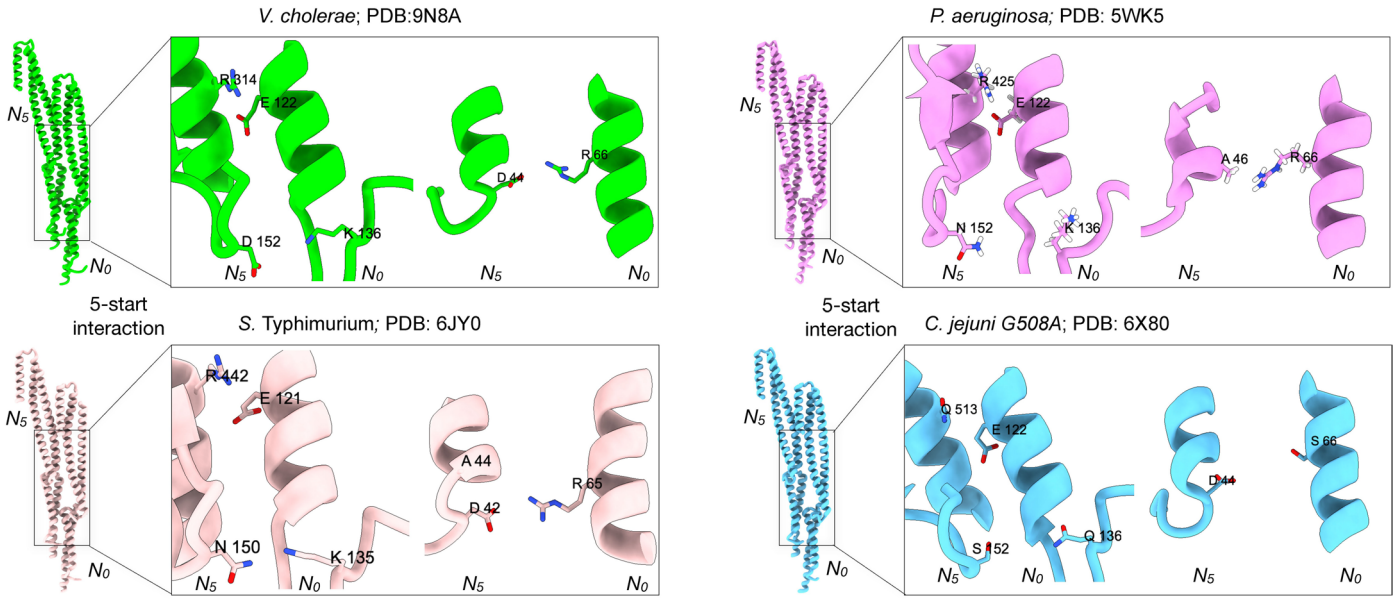

Extended Data Fig. 6 | Interdomain interactions along the 5-start interface across bacterial species. Our *V. cholerae* filament model presents three potential interaction pairs: $E122_0$-$R314_5$, $K136_0$-$D152_5$, and $R66_0$-$D44_5$. Similar interactions are observed in other bacterial species, such as *S.* Typhimurium[15] ($K135_0$ and $N150_5$, $E121_0$ and $R442_5$, $R65_0$ and $D42_5$), *P. aeruginosa*[27] ($E122_0$ and$R425_5$, and $R66_0$ and $A46_5$), and *C. jejuni*[29] ($E122_0$ and $Q513_5$, and $Q136_0$ and $S152_5$).

https://doi.org/10.1038/s41564-025-02161-x

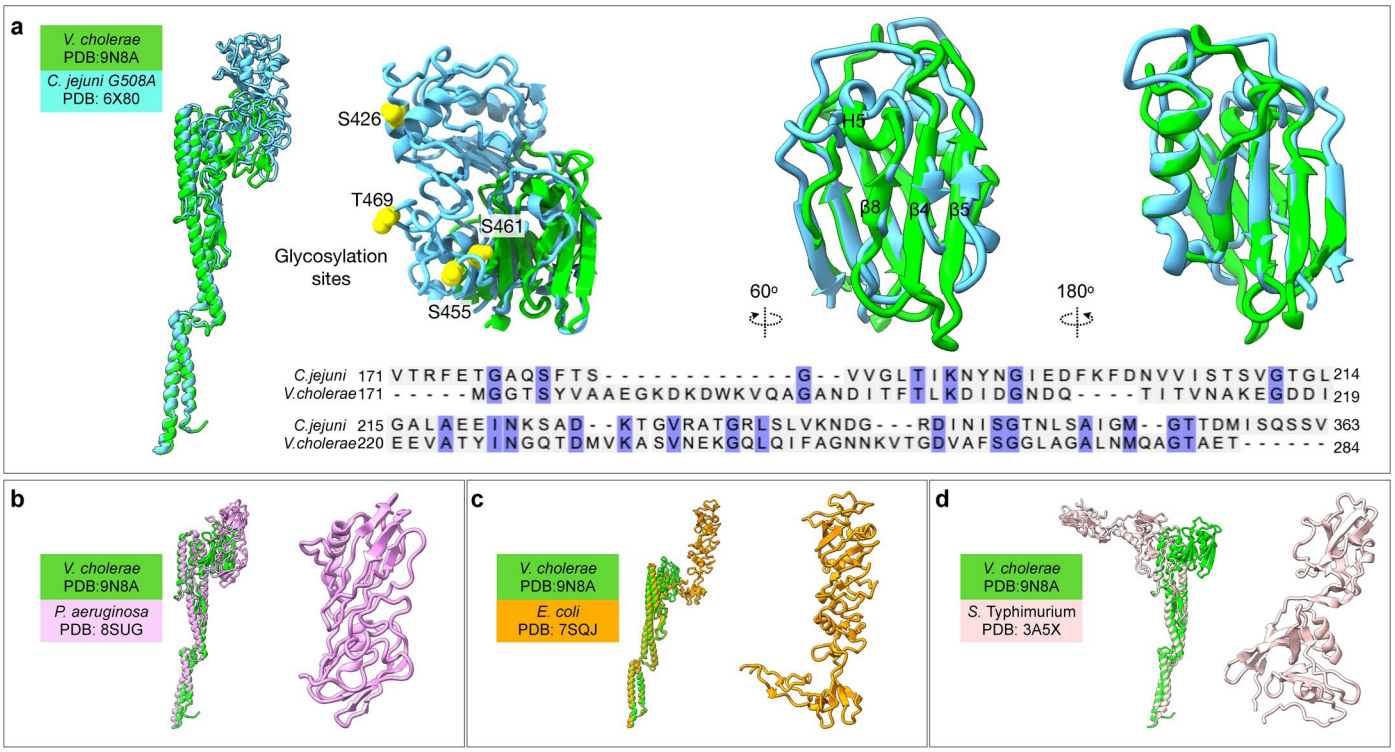

Extended Data Fig. 7 | Comparison of FlaD from *V. cholerae* with flagellins from other bacteria. (a) The *C. jejuni* flagellin (PDB:6×80)[29] has a three-stranded β-sheet and helix motif similar to that in *V. cholerae* flagellin FlaD, which is shielded by the outer surface of glycosylation sites. This motif was not observed in *P. aeruginosa* PAO1[27] (**b**), *E. coli*[14] (**c**), or *S.* Typhimurium[15] (**d**).

https://doi.org/10.1038/s41564-025-02161-x

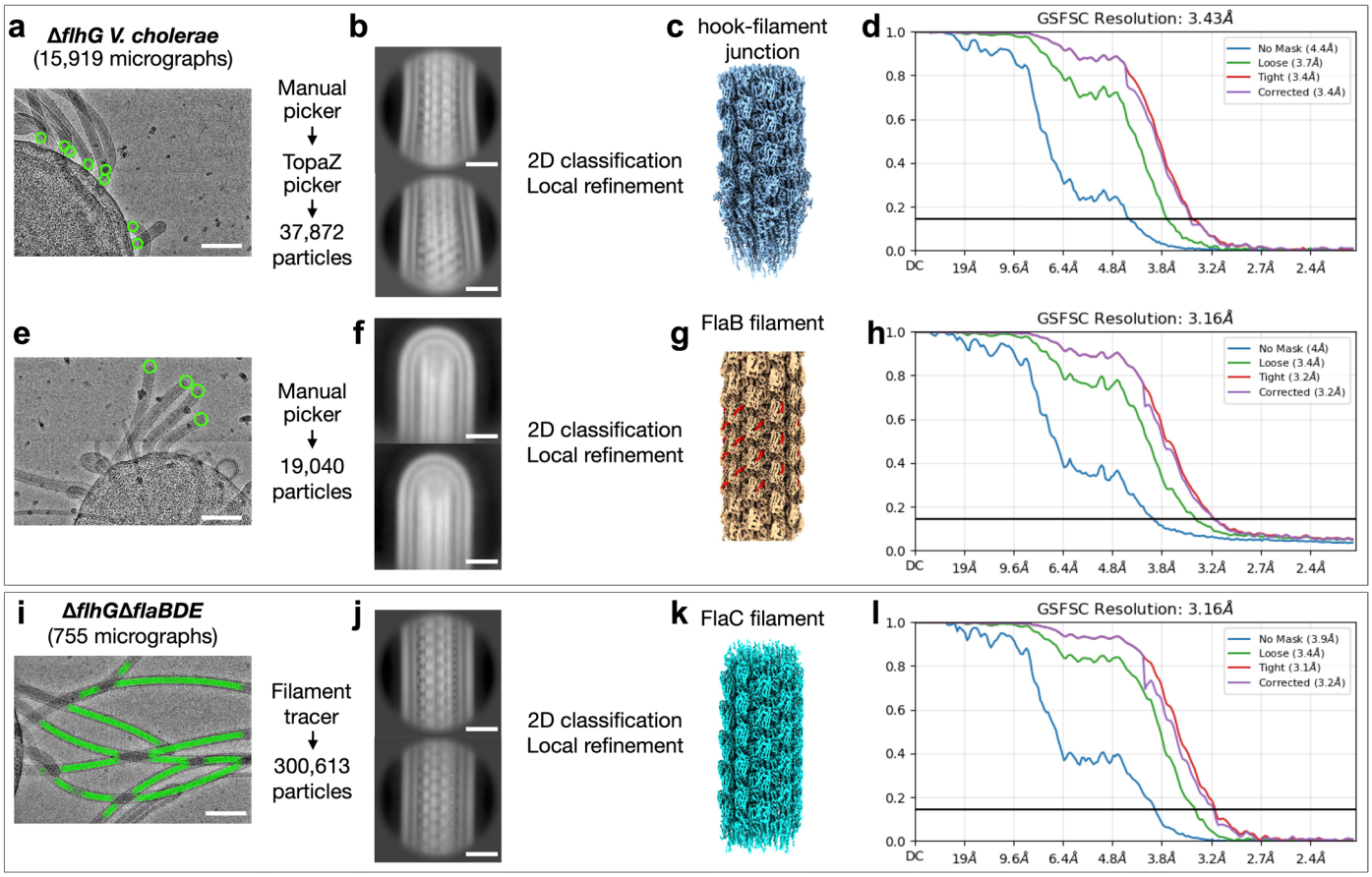

Extended Data Fig. 8 | CryoSPARC workflow for structural determination of the FlaA, FlaB, and FlaC filament in *V. cholerae*. **(a)** 15,919 micrographs of Δ*flhG V. cholerae* were collected to determine the FlaA filament structure. Scale bar: 100 nm. **(b)** Representative 2D classifications of the hook–filament junction region after manual picking and Topaz picker[30]. Scale bar: 200 Å. **(c, d)** Cryo-EM density map of the hook–filament junction with FlaA filament, resolved at 3.43 Å based on the "gold standard" $FSC_{0.143}$ plot. **(e)** Snapshot of manual picking at the filament tip region. Scale bar: 100 nm. **(f)** Representative 2D classifications of filament tip particles from 19,040 manually picked particles. Scale bar: 200 Å. **(g, h)** Cryo-EM density map of the FlaB filament at the filament tip, resolved at 3.16 Å. **(i)** Snapshot of filament tracer in Δ*flhGΔflaBDE V. cholerae*. Scale bar: 100 nm. **(j)** Representative 2D classifications of the FlaC filament. Scale bar: 200 Å. **(k, l)** Cryo-EM density map of the FlaC filament in Δ*flhGΔflaBDE V. cholerae*, resolved at 3.16 Å.

https://doi.org/10.1038/s41564-025-02161-x

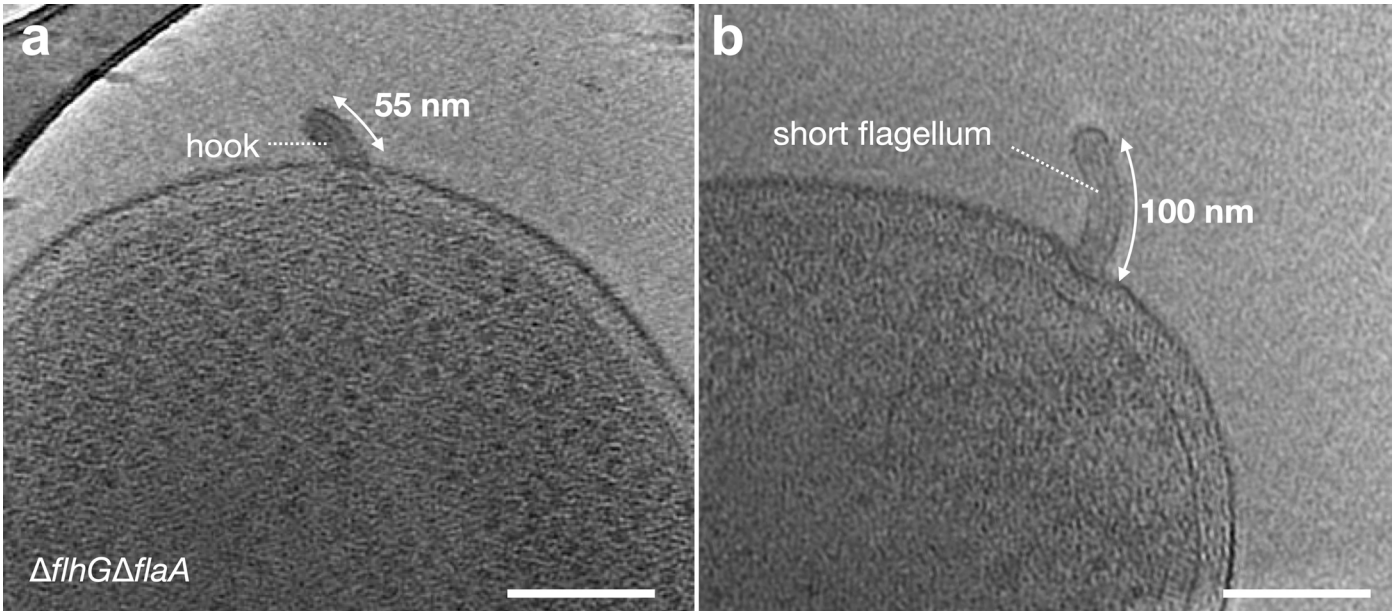

Extended Data Fig. 9 | Cryo-ET reconstructions of the Δ*flhG*Δ*flaA* cell poles. (a) A slide shows a 55 nm flagellar hook. **(b)** A slide shows a short flagellum 100 nm in length.

https://doi.org/10.1038/s41564-025-02161-x

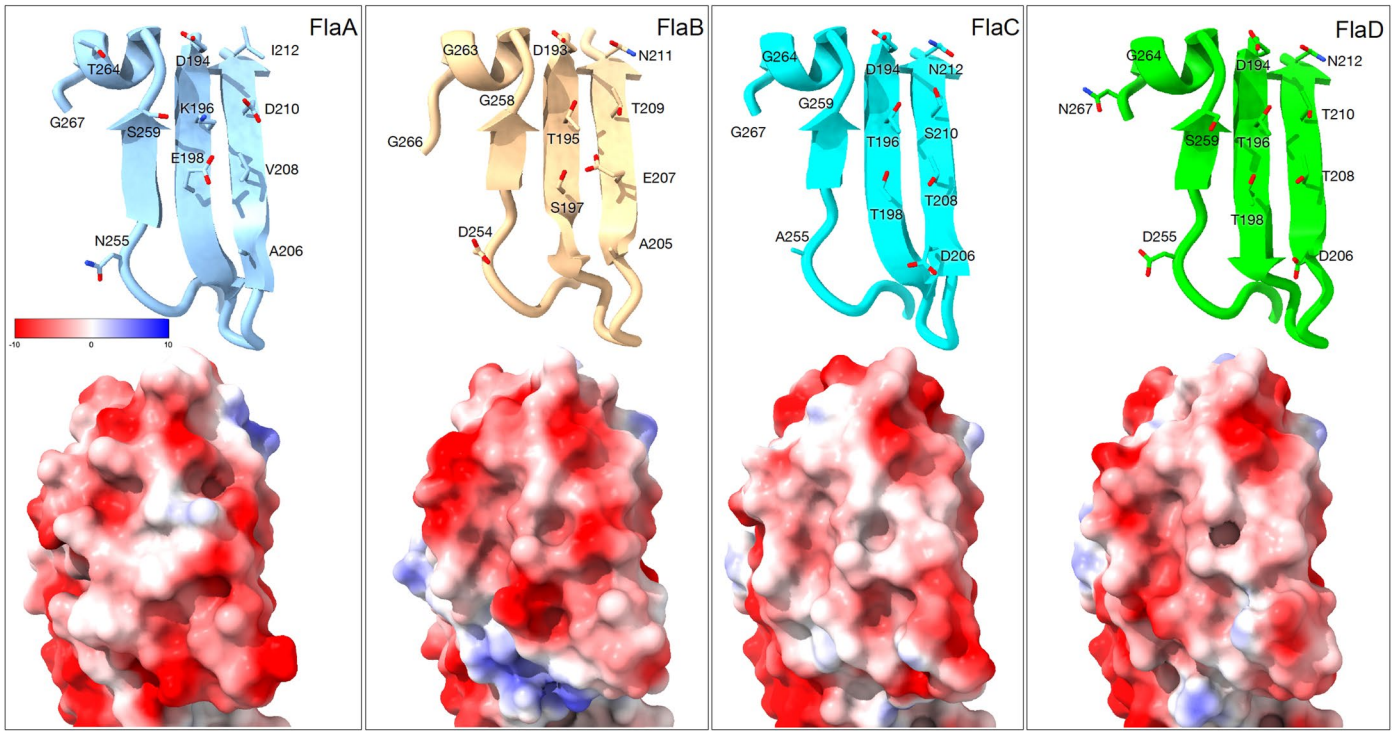

Extended Data Fig. 10 | The three-stranded β-sheet and helix motif on the filament surface are conserved across four flagellins in *V. cholerae*. Four flagellins share similar morphology (top panels) and charged surfaces (bottom panels).

nature portfolio

Corresponding author(s): Wangbiao Guo & Jun Liu

Last updated by author(s): 9/17/2025

Reporting Summary

Nature Portfolio wishes to improve the reproducibility of the work that we publish. This form provides structure for consistency and transparency in reporting. For further information on Nature Portfolio policies, see our Editorial Policies and the Editorial Policy Checklist.

Statistics

For all statistical analyses, confirm that the following items are present in the figure legend, table legend, main text, or Methods section.

n/a	Confirmed	
☐	☒	The exact sample size (*n*) for each experimental group/condition, given as a discrete number and unit of measurement
☐	☒	A statement on whether measurements were taken from distinct samples or whether the same sample was measured repeatedly
☒	☐	The statistical test(s) used AND whether they are one- or two-sided *Only common tests should be described solely by name; describe more complex techniques in the Methods section.*
☒	☐	A description of all covariates tested
☒	☐	A description of any assumptions or corrections, such as tests of normality and adjustment for multiple comparisons
☒	☐	A full description of the statistical parameters including central tendency (e.g. means) or other basic estimates (e.g. regression coefficient) AND variation (e.g. standard deviation) or associated estimates of uncertainty (e.g. confidence intervals)
☒	☐	For null hypothesis testing, the test statistic (e.g. *F*, *t*, *r*) with confidence intervals, effect sizes, degrees of freedom and *P* value noted *Give P values as exact values whenever suitable.*
☒	☐	For Bayesian analysis, information on the choice of priors and Markov chain Monte Carlo settings
☒	☐	For hierarchical and complex designs, identification of the appropriate level for tests and full reporting of outcomes
☒	☐	Estimates of effect sizes (e.g. Cohen's *d*, Pearson's *r*), indicating how they were calculated

Our web collection on statistics for biologists contains articles on many of the points above.

Software and code

Policy information about availability of computer code

Data collection	Cryo-EM: SerialEM3.7
Data analysis	Cryo-EM:MotionCor2, CTFFIND4, Cryosparcv4.6, PSIPRED4.0, AlphaFold2/3, Coot0.9.8.1, Phenix1.20.1, ChimeraX1.9, Structure comparison and structure-based sequence alignment:Dali,

For manuscripts utilizing custom algorithms or software that are central to the research but not yet described in published literature, software must be made available to editors and reviewers. We strongly encourage code deposition in a community repository (e.g. GitHub). See the Nature Portfolio guidelines for submitting code & software for further information.

Data

Policy information about availability of data

All manuscripts must include a data availability statement. This statement should provide the following information, where applicable:

- Accession codes, unique identifiers, or web links for publicly available datasets
- A description of any restrictions on data availability
- For clinical datasets or third party data, please ensure that the statement adheres to our policy

The atomic coordinates of the FlaD model for the helical non-sheathed flagellar filament (PDB: 9N8B), helical sheathed flagellar filament (PDB: 9N8H), asymmetrical sheathed FlaD filament (PDB: 9N8A), and FlaA filament (PDB: 9N8G) in ΔflhG V. cholerae have been deposited in the Protein Data Bank (PDB). The corresponding

density maps for the helical non-sheathed flagellar filament (EMD-49126), helical sheathed flagellar filament (EMD-49129), asymmetrical sheathed FlaD filament (EMD-49125), and FlaA filament (EMD-49128) have been deposited in the Electron Microscopy Data Bank (EMDB). Additionally, the FlaC model and density map of the asymmetrical sheathed straight flagellar filament in ΔflhGΔflaBDE have been deposited in the PDB (PDB: 9N8M) and EMDB (EMD-49131).

Research involving human participants, their data, or biological material

Policy information about studies with human participants or human data. See also policy information about sex, gender (identity/presentation), and sexual orientation and race, ethnicity and racism.

Reporting on sex and gender	N/A
Reporting on race, ethnicity, or other socially relevant groupings	N/A
Population characteristics	N/A
Recruitment	N/A
Ethics oversight	N/A

Note that full information on the approval of the study protocol must also be provided in the manuscript.

Field-specific reporting

Please select the one below that is the best fit for your research. If you are not sure, read the appropriate sections before making your selection.

☒ Life sciences ☐ Behavioural & social sciences ☐ Ecological, evolutionary & environmental sciences

For a reference copy of the document with all sections, see nature.com/documents/nr-reporting-summary-flat.pdf

Life sciences study design

All studies must disclose on these points even when the disclosure is negative.

Sample size	A total of 18,064 micrographs were collected from ΔflhG cells and 755 micrographs were captured from ΔflhGΔflaBDE cells. 103,479 particles lacking the sheath were intially identified from 1,132,628 particles after 2D classification. Ultimately, the final helical reconstruction map of non-sheathed flagellar filament achieved a near-atomic resolution of 2.45 Å. 11,715 particles exhibited distinct curvature. These particles were selected and re-extracted with 1280 box size to visualize its curvature. We acquired 15,919 cryo-EM micrographs from ΔflhG V. cholerae cells. We selected 37,872 particles located in the hook-filament junction. Eventually, we determined the structure of FlaA flagellin at 3.43 Å resolution.
Data exclusions	Cryo-EM particles with poor quality or irrelevant features were excluded during 2D and 3D classification. This standard procedure is widely used to obtain high-resolution cryo-EM structures of biomacromolecules.
Replication	All attempts at replication were successful.
Randomization	Randomization was not applicable to this study.
Blinding	Blinding was not applicable in this study.

Reporting for specific materials, systems and methods

We require information from authors about some types of materials, experimental systems and methods used in many studies. Here, indicate whether each material, system or method listed is relevant to your study. If you are not sure if a list item applies to your research, read the appropriate section before selecting a response.

Materials & experimental systems

n/a	Involved in the study
☒	☐ Antibodies
☒	☐ Eukaryotic cell lines
☒	☐ Palaeontology and archaeology
☒	☐ Animals and other organisms
☒	☐ Clinical data
☒	☐ Dual use research of concern
☒	☐ Plants

Methods

n/a	Involved in the study
☒	☐ ChIP-seq
☒	☐ Flow cytometry
☒	☐ MRI-based neuroimaging

Plants

Seed stocks	N/A
Novel plant genotypes	N/A
Authentication	N/A